Biophysical*Journal*
Article

Biophysical Society

Insights into the Cooperative Nature of ATP Hydrolysis in Actin Filaments

Harshwardhan H. Katkar,[1] Aram Davtyan,[1] Aleksander E. P. Durumeric,[1] Glen M. Hocky,[1] Anthony C. Schramm,[2] Enrique M. De La Cruz,[2] and Gregory A. Voth[1,*]
[1]Department of Chemistry, Institute for Biophysical Dynamics and James Frank Institute, University of Chicago, Chicago, Illinois and [2]Department of Molecular Biophysics and Biochemistry, Yale University, New Haven, Connecticut

ABSTRACT Actin filaments continually assemble and disassemble within a cell. Assembled filaments "age" as a bound nucleotide ATP within each actin subunit quickly hydrolyzes followed by a slower release of the phosphate P_i, leaving behind a bound ADP. This subtle change in nucleotide state of actin subunits affects filament rigidity as well as its interactions with binding partners. We present here a systematic multiscale ultra-coarse-graining approach that provides a computationally efficient way to simulate a long actin filament undergoing ATP hydrolysis and phosphate-release reactions while systematically taking into account available atomistic details. The slower conformational changes and their dependence on the chemical reactions are simulated with the ultra-coarse-graining model by assigning internal states to the coarse-grained sites. Each state is represented by a unique potential surface of a local heterogeneous elastic network. Internal states undergo stochastic transitions that are coupled to conformations of the underlying molecular system. The model reproduces mechanical properties of the filament and allows us to study whether conformational fluctuations in actin subunits produce cooperative filament aging. We find that the nucleotide states of neighboring subunits modulate the reaction kinetics, implying cooperativity in ATP hydrolysis and P_i release. We further systematically coarse grain the system into a Markov state model that incorporates assembly and disassembly, facilitating a direct comparison with previously published models. We find that cooperativity in ATP hydrolysis and P_i release significantly affects the filament growth dynamics only near the critical G-actin concentration, whereas far from it, both cooperative and random mechanisms show similar growth dynamics. In contrast, filament composition in terms of the bound nucleotide distribution varies significantly at all monomer concentrations studied. These results provide new insights, to our knowledge, into the cooperative nature of ATP hydrolysis and P_i release and the implications it has for actin filament properties, providing novel predictions for future experimental studies.

INTRODUCTION

Actin is a major component of the eukaryotic cytoskeleton and has important functions in cell motility and division. The monomeric form, globular actin (G-actin), polymerizes into filamentous actin (F-actin) and associates with filament-binding proteins to form dynamic filaments of various architectures that are meticulously regulated to perform these functions. Actin monomers are large single-domain proteins made of 375 amino acids, and they contain a bound nucleotide at their center. The nonpolymerized G-actin in the cell is predominantly found in an ATP-bound state (1). Polymerization of actin is followed by actin-catalyzed hydrolysis of the bound nucleotide ATP, and the hydrolysis in F-actin subunits has been estimated to be >40,000 times faster than in G-actin owing to the structural changes that G-actin undergoes as it transforms into an F-actin upon polymerization, during which it becomes more planar (2–6).

An actin monomer is not symmetric, and the actin filaments are polar in nature. New actin monomers predominantly add at the "barbed" end of the filament and have a faster rate of depolymerization at the "pointed" end (7). Depending upon the G-actin concentration in the local environment, a filament can either grow from both ends (high concentration), shrink at both ends (low concentration), or grow at the barbed end while shrinking at the pointed end. At a particular concentration, these two rates are balanced and filaments undergo treadmilling, whereby a constant filament length is maintained on average. Experimental evidence suggests that incorporation of a new actin monomer into the filament does not immediately induce ATP hydrolysis, nor does hydrolysis have to occur for subsequent monomers to be added (8). It is also believed that the rate of exchange of nucleotides in a filament with those in solution is negligible (9,10). Instead, ATP is predominantly

---

Submitted May 11, 2018, and accepted for publication August 22, 2018.

*Correspondence: gavoth@uchicago.edu

Editor: David Sept.
https://doi.org/10.1016/j.bpj.2018.08.034

incorporated into the filament through polymerization of ATP-bound G-actin. The interplay of polymerization and hydrolysis results in a time lag associated with the hydrolysis in the filament with respect to polymerization and hence results in an ATP-bound cap in filaments at high G-actin concentration (11,12). In F-actin, the hydrolysis of ATP to form ADP is not direct (11) but proceeds as a fast conversion to ADP with a protein-bound inorganic phosphate (ADP-P_i), followed by a slow release of the inorganic phosphate to the solution (13–16). ATP hydrolysis occurs on a timescale of seconds, whereas P_i release takes place over minutes (2,7,13,14,17).

There are multiple cation-binding sites in actin with varying affinities that modulate the mechanical properties of the filament (12,18–21). Additionally, the state of the bound nucleotide also strongly influences its mechanical properties. The persistence length of actin filaments decreases as the bound nucleotide changes from ATP to ADP, as shown from experimental measurements (22). Recent simulation work also predicts that the bound nucleotide state affects the response of G-actin to various applied stresses (23).

Simplified mechanistic models parameterized using a top-down approach, in which model parameters are tuned to obtain certain target filament properties, have been successfully used to study actin filaments and their mechanical properties (24,25). Such models reduce large-scale complex processes into simpler phenomenology but typically have somewhat limited predictive power and can potentially lack a rigorous justification for the choice of parameters involved. On the other hand, bottom-up coarse-grained (CG) models of actin filaments that are parameterized into a heteroelastic network (26) by using reference all-atom simulations have been found to be adequate in capturing actin filament mechanical properties as a function of the state of the nucleotides even at a highly coarse resolution of four CG sites per actin subunit (27,28). A CG model with twelve CG sites per actin subunit has been shown to capture several other important structural aspects of actin (29). Such models that use a particle representation with an associated pairwise effective interaction potential are, however, often limited in their ability to represent certain molecular changes, including chemical or structural changes, that cannot be represented at the resolution of the CG sites, even if such changes ultimately affect the system behavior at the resolution of the CG model. Moreover, the underlying atomistic simulations further limit the configurations that such CG models can explore, as only configurations sampled by the atomistic model inform the effective potential, "locking" the CG model to, e.g., a given nucleotide composition. An example of such configurational changes is the state of the nucleotide bound to actin subunits in a filament. Although the CG particle representation has been shown to capture many essential conformational changes in actin subunits conditional on the state of bound nucleotide, these CG models do not offer insight about the hydrolysis dynamics involved, primarily because neither ATP hydrolysis nor P_i release are realized in all-atom simulations because of the timescales involved.

In contrast to the CG particle representation, a bottom-up model can be constructed using a discrete state representation, characterized by instantaneous transitions between different configurational states; these models are termed Markov state models (MSMs) (30–33). Generally, the rates governing the behavior of MSMs are obtained through statistics derived from fine-grained all-atom simulations. Bottom-up MSMs are traditionally only able to study systems for which statistics have been directly obtained (32,34,35); including other states or rates in the model requires the computational scientist to use additional knowledge to determine the modified rate coefficients.

In this work, we first utilized the emerging concept of the ultra-coarse-grained (UCG) model, which combines both the particle and discrete state representations in a systematic way by defining an internal state associated with the CG particles (36–39). The internal states of the CG particles can in principle account for any reactions or conformational changes within the CG particles, making the UCG model ideal for actin filaments to study ATP hydrolysis and P_i release reactions. The UCG model was then used to systematically parametrize an MSM, which was analyzed to make conclusions about the spatial cooperativity present in an actin filament.

The macroscopic rates of the polymerization, depolymerization, ATP hydrolysis, and P_i release reactions have been measured indirectly from experiments using fluorescence labeling, radioactive labeling, etc., by assuming an underlying kinetic model (9–11,13,17,40,41). In experiments involving a conserved system, in which the total mass of actin (G-actin + F-actin) in the system remains constant throughout the experiment, a characteristic sigmoidal-shaped curve is obtained for time evolution of filament growth and ATP hydrolysis, showing that hydrolysis lags behind the polymerization at high initial G-actin concentrations (13,42). Since it was established that ATP hydrolysis is decoupled from polymerization, there have been two major classes of hydrolysis models in the literature: the random model and the cooperative model. The random hydrolysis model (11,34), first proposed before the intermediate ADP-P_i was discovered, assumes that ATP bound to any F-actin subunit throughout the filament hydrolyzes at the same rate. Indirectly, this implies that the conformation of the neighboring subunits does not significantly affect the rate of hydrolysis, as the neighboring nucleotide state modulates the local conformational sampling of each monomer. Alternatively, the nucleotide state of neighboring subunits could modulate the rate constant, as is assumed in the cooperative hydrolysis models. Among the cooperative models, the vectorial model is the most distinct from the random hydrolysis model because it assumes that ATP hydrolysis can occur predominantly in those subunits in the filament that have an adjoining ADP subunit and hence are at an ATP/ADP (or ATP/ADP-P_i) interface. In the strictest version of the vectorial model (35,43), at the most two interfaces (exactly two if the filament is growing from both its ends) can exist in a filament because hydrolysis is assumed to occur exclusively at the ATP/ADP interface and the interface simply moves toward the growing end of the filament as time progresses. The more realistic version of the vectorial model (cooperative model) assigns a relatively small nonzero hydrolysis rate for ATP subunits that are not present at the interface (8,44).

There have been a number of studies attempting to perform a systematic comparison between the two classes of models (8,35,42,45–47). However, common experimentally measured quantities such as rate of filament elongation, fluctuations in filament length, and size of unhydrolyzed ATP cap near the filament end are found to be insensitive to the mechanism of hydrolysis over a wide range of G-actin concentration, with small quantitative difference very close to the critical concentration (35,47). A mixture of ATP-bound G-actin and ADP-bound G-actin can be used to introduce a different number of ATP-ADP interfaces in the filament by varying the composition of the mixture, thereby providing a way of enhancing the effective rate of hydrolysis within the context of the vectorial model (42). Fitting the predictions of a cooperative model to the time course of polymerization and ATP hydrolysis measured in these experiments eliminates the possibility of the strict vectorial model being accurate in all cases and suggests that the rate of hydrolysis at the ATP-ADP interface must be less than 100 times faster than the rate of hydrolysis away from the interface, although the predictions of a random hydrolysis mechanism were also shown to be able to explain the observed experimental data (42,46). By using the nearest-neighbor cooperativity in such a model as a parameter to fit experimentally measured P_i release profiles, it was shown that the possibility of a high degree of cooperativity in P_i release could not be completely excluded, however, with some ambiguity in the data analysis involved (41,44,48,49). The random and vectorial models are based on two simple microscopic physical hypotheses that are able to accurately explain the experimental observations. An intermediate model could be constructed by assuming a more complex cooperativity that goes beyond the two-body binary cooperativity (two possible hydrolysis rates, one at the interface and one away from the interface) previously used in the vectorial and cooperative models. However, lack of any direct experimental evidence differentiating these hypotheses makes empirically justifying and parameterizing such a complex cooperative model difficult. The central contribution of this manuscript is the prediction of the nature and extent of such complex cooperativity present in both ATP hydrolysis and P_i release reactions using a systematic CG modeling framework. As described below, this prediction was obtained through a multiscale CG approach that involved making careful assumptions, and it was constructed with all-atom molecular dynamics simulations at its foundation. Hence, the UCG model was essentially limited by the accuracy of the atomistic force field and the assumptions made.

Our UCG model, derived from all-atom (AA) molecular dynamics simulations, is able to provide a complex but detailed physical picture of the ATP hydrolysis and P_i release processes based on the behavior produced by a general atomistic force field (CHARMM27 + CMAP (50)). We constructed a UCG model that serves as a good representation of an actin filament at a low resolution and also, for the first time to our knowledge, takes into account the nucleotide state of each actin subunit explicitly. The UCG filament model and conformational coupling between subunits was derived via a systematic procedure from AA molecular dynamics simulations, whereas the instantaneous conformation-dependent rates of state transitions were approximated based on physical principles and implemented via a stochastic-state hopping procedure with resulting macroscopic rates tied to experimental observations. After ensuring that the UCG model provided reasonable predictions for the mechanical properties of the filament, an MSM was constructed at the coarse resolution of traditional biological models. In the MSM, only the nucleotide composition along the position of subunits in the filament was retained, whereas conformational fluctuations were integrated out. The model did not explicitly impose any cooperativity with respect to the nucleotide composition of neighboring subunits but was instead able to predict the spatial dependence of ATP hydrolysis and P_i release in actin filaments, allowing us to directly compare results with established hydrolysis models in the literature. Finally, the MSM was extended using experimental knowledge to explore the effects of concurrent hydrolysis and polymerization and used to compare the implications of the predicted cooperativity by modifying two representative models proposed in (34,47).

METHODS

CG model

Our modeling approach is fundamentally based on using AA molecular dynamics simulations as the primary basis for constructing lower resolution CG models. The configurational behavior of the CG model of the filament conditional on nucleotide composition was parameterized in two steps: 1) using a systematic map to reduce the AA structure to fewer CG sites or “beads” (see Fig. 1), and 2) using mapped system distributions to construct a CG effective force field that governs the conformations of those CG beads in such a way that the AA behavior is faithfully reproduced. An essential feature of the UCG model in the current context is then the assignment of additional discrete internal states to the CG beads, with a different CG force field associated with each state. In actin, for example, we used this additional model flexibility to represent the states of the bound nucleotide. The CG F-actin filament dynamics were then modeled using continuous-time Langevin dynamics simulations of the CG beads using appropriate force fields based on the instantaneous set of internal states of the

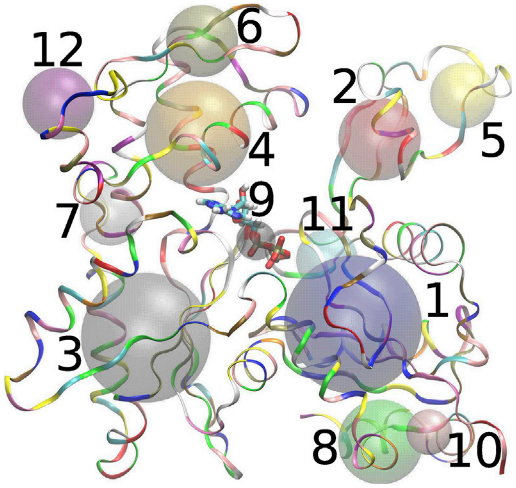

FIGURE 1 Schematic showing the CG mapping used in our study. The atomistic structure of ADP-P_i bound actin subunit is shown as ribbons, with the corresponding CG sites shown as beads. CG bead indices 1–12 are marked next to each CG site. Our final model has five major beads corresponding to CG sites with indices 1–5. To see this figure in color, go online.

neighboring CG beads, in addition to allowing discrete jumps between the various internal states. In other words, kinetics of ATP hydrolysis or P_i release in a subunit is controlled by the rates governing the switching between these states, which inherently must also take into account the conformational changes that the subunit undergoes upon hydrolysis or P_i release and additionally take into account the interdependence on the nucleotide states of its neighboring subunits. It is important to note that the latter significantly increases the complexity of the problem, and to make progress, we must invoke certain assumptions. Firstly, we restricted the CG force field to pairwise interactions and imposed a degree of locality on these interactions. As described in (36), without the locality approximation, there is an exponentially large number of possible states to consider, making the UCG approach infeasible. The local nature of the interactions is somewhat based on biological intuition. Second, we constructed the CG force field from AA simulations only for actin filaments consisting of subunits with identical nucleotides and used a simple mixing rule to construct the CG force field otherwise. A justification for the mixing rule is provided in the Supporting Materials and Methods. The details of the AA simulations are also described in the Supporting Materials and Methods. Briefly, a periodic 13-subunit actin filament was constructed using the Oda structure for each state of the bound nucleotide (29,50–56). Three AA simulation trajectories were obtained, one for a pure ATP-bound actin filament, one for a pure ADP-P_i-bound actin filament, and one for a pure ADP-bound actin filament. Each of these AA trajectories was used to obtain CG models for the filaments with corresponding states of the bound nucleotide. The UCG force field and the UCG discrete state-switching algorithm are described below.

UCG force field

Each of the ATP-, ADP-P_i-, and ADP-bound states of actin filament were independently coarse grained using a 12-site mapping (29,57) (Fig. 1) and a hybrid force field. The hybrid force field consisted of an intrasubunit heterogeneous elastic network model (hENM (27)) and an intersubunit pairwise interaction modeled with an inverted Gaussian potential, which will allow for future studies to include (de)polymerization at the UCG resolution. The details of these potentials are provided in the Supporting Materials and Methods. First, AA simulation trajectories of an actin filament with 13 subunits (bound exclusively with either ATP, ADP-P_i, or ADP) were used to generate a force field for a filament in a pure nucleotide state. To build the hybrid model, we started by connecting all pairs of intrasubunit beads by springs. We then connected intersubunit beads with springs, but to simplify the conversion of intersubunit interactions to be dissociable, we chose to only include springs between a subset of CG sites that we call “major beads” and restricted these intersubunit springs to bead pairs that are less than three actin subunits apart to help enforce the locality of UCG interactions discussed earlier. Finally, we used the hENM procedure to assign spring constants that maximally match the fluctuations in the AA trajectory. To choose which CG sites to use for intersubunit interactions, we tested varying numbers of major beads, adding them in increasing order of their CG index as labeled in Fig. 1. A model including the first five beads as major beads was chosen based on physical considerations (important domains in actin that mediate intersubunit interactions) and because it gave the best agreement in persistence length (22,27,28,58–63) (see Supporting Materials and Methods for details). The five major beads in an actin subunit correspond to the four major subdomains in actin and the D-loop region (Fig. 1). The D-loop region inserts into actin’s barbed end “target binding cleft” and is an important mediator of longitudinal interactions in the filament (20,56,59,64–67).

After the hENM procedure, the intersubunit springs between actin monomers in the filament were converted into soft potentials. This was done by converting each intersubunit elastic spring potential into an inverted Gaussian potential by least-square fitting to the elastic-spring-potential well in the region corresponding to a well depth of 3 kcal/mol. The well depth was set to be strong enough to prevent adjacent subunits in a filament from leaving the filament but weak enough to prevent any large jumps in energy of the system that would lead to large numerical integration errors.

The intersubunit inverted Gaussian potential for a pair of CG beads with distinct states (e.g., ATP:ADP-P_i) of the bound nucleotide was obtained using a simple mixing rule that involved averaging parameters of the potential for each of the individual pure states (ATP:ATP and ADP-P_i:ADP-P_i), as described in the Supporting Materials and Methods. All UCG simulations were performed in the Large-scale Atomic/Molecular Massively Parallel Simulator Molecular Dynamics software (68).

UCG state switching

Each of the actin subunits was assigned an internal state depending on its bound nucleotide. The ATP hydrolysis and P_i release reactions were then represented as switching of these internal states (37). The simulation methodology consisted of evolving continuous variables (positions, velocities of CG beads) using Langevin dynamics along with discrete state transitions. Physically, these discrete transitions correspond to either hydrolysis or phosphate release, with the instantaneous rate an expression of how the barrier of the reaction changes depending on the instantaneous configuration of the filament. The nature of this dependence indirectly produces all hydrolysis and phosphate release cooperativity observed in the current study.

However, full rigorous parametrization of this dependence, either through experimental data or reactive atomistic simulation, is infeasible. Experimental data cannot achieve the required resolution, and a reactive atomistic simulation is computationally prohibitive when considering the dependence of a complex reaction on a multitude of protein environments. Instead, simple arguments on the transition state stability as a function of the reactants or product stability were used. Fundamentally, the approach is similar to kinetic implications of the Hammond postulate: the free energy of the transition state has approximately the same dependence on configuration as either the products or reactants, depending on which of the products or reactants is closer in free energy to the transition state (see Supporting Materials and Methods for an additional discussion) (69–72). Additional dependence of the transition state free energy on the local configuration, such as the dihedral angle of the monomeric unit, was introduced through terms $k(\phi)$ in the equations below. This approach resulted in the following instantaneous rate expressions. For a given subunit initially in the state i, the instantaneous rate of switching to state j is given by the following equation based on the Metropolis-Hastings-like criterion

$$\begin{aligned} K_{i\to j} &= k_{i\to j}(\phi)\mathrm{Min}\left[\frac{k_{j\to i}(\phi)}{k_{i\to j}(\phi)}\exp\left[-\beta\left(U_j - U_i\right) - \varepsilon_{ij}\right], 1\right] \\ &\equiv k_{i\to j}(\phi)p_{i\to j}, \end{aligned} \tag{1}$$

where

$$k_{i\to j}(\phi) = k^0_{i\to j}[0.5 + 0.5\tanh(\eta(\phi - \phi_0))]. \tag{2}$$

Here, $U_j - U_i$ is the energy difference between states j and i, $\phi - \phi_0$ is the difference between the instantaneous dihedral angle between CG beads 2-1-3-4 of the subunit and its average value in state i, and η is the parameter that controls the explicit dihedral angle dependence, whereas $k^0_{i\to j}$ and ε_{ij} are model parameters. Computationally, the prefactor $k_{i\,\to\,j}(\phi)$ can be seen as specifying the rate of attempting a state transition, and $p_{i\,\to\,j}$ gives the probability of accepting the transition. As the transition describes a chemical reaction in an equilibrium system, detailed balance implies that the rate for the reverse reaction, in which a subunit initially in state j switches to state i, is given by

$$K_{j\to i} = k_{j\to i}(\phi)\mathrm{Min}\left[\frac{k_{i\to j}(\phi)}{k_{j\to i}(\phi)}\exp\left[-\beta\left(U_i - U_j\right) + \varepsilon_{ij}\right], 1\right], \tag{3}$$

where

$$k_{j\to i}(\phi) = k^0_{j\to i}[0.5 - 0.5\tanh(\eta(\phi - \phi_0))]. \tag{4}$$

The explicit dihedral angle dependence was modeled as a smooth step function such that it resulted into an increase in $k_{i\,\to\,j}(\phi)$ for the forward reaction and decrease in $k_{j\,\to\,i}(\phi)$for the reverse reaction as the dihedral angle ϕ increases. The explicit dihedral angle dependence was based on our previous work (4–6), which attributes the increase in rate of hydrolysis to the flattening of the actin subunit. We set $\phi_0 = -10^\circ$ and used $\eta = 0.125$ for the ATP hydrolysis reaction but turned off the explicit dihedral angle dependence for the P_i release reaction by setting $\eta = 0$ (73). Additional discussion of the physical meaning of these parameters can be found in the Supporting Materials and Methods.

Parameter estimation

The parameters $k^0_{i\to j}$, $k^0_{j\to i}$, and ε_{ij} are the UCG model parameters that need to be estimated. These were optimized using the following three conditions. The instantaneous forward and reverse reaction rates, on average, must match the known macroscopic reaction rates. This provides two conditions, one for the forward reaction and one for the reverse reaction. These two conditions were specified by the system being simulated. The third condition has more freedom in its choice, and we selected this condition such that the average acceptance probability for the forward reaction had a desired value. The motivation behind this choice was that it provides a handle to control the sensitivity of state transitions to the energy difference ($U_i - U_j$) between the two states. The details of parameter estimation are provided in the Supporting Materials and Methods (5,6,74,75). In the final model, we set the average acceptance probability to 0.01 for both ATP hydrolysis and P_i release reactions.

Markov state model

The UCG simulations performed were analyzed through their behavior at the resolution of an MSM. The MSM resolution was based on the kinetic models used in the literature (34,47). In this MSM description, an actin filament contains no configurational behavior; we only considered the length of actin filaments and their composition in terms of the nucleotide state. In other words, the actin filament system was represented by a state vector, with positions of elements of the vector corresponding to positions of actin subunits in a filament and the value of each element (ATP, ADP-P_i, or ADP) corresponding to the state of the nucleotide bound to the respective subunit. Mean first passage times were estimated using the mapped statistics observed in the UCG simulations and were used to parameterize the MSM. This procedure is described in more detail in the next section.

The MSM model was further extended to include polymerization and depolymerization of actin subunits. Note that we ignored any modified hydrolysis or phosphate release behavior at the ends of the filament in our MSM for simplicity. For example, the P_i release rate in the terminal subunits at the filament ends has been predicted to be different than that in the interior of the filament (40,41), which we did not express in our model. We additionally ignored any multibody cooperative effects on the rates of polymerization and depolymerization at the two ends of the filament. As the addition of ATP-bound actin to the filament introduces energy into the local system represented by the MSM, the constraint of detailed balance was not imposed when considering the transitions related to the addition or removal of actin units. As a result, when considering polymerization, the length of the state vector at a given instant was equal to the length of the filament at that instant, and the two terminal positions of the state vector corresponded to the barbed and pointed ends of the filament. Polymerization (depolymerization) at the ends resulted in expansion (shrinking) of the state vector, whereas ATP hydrolysis and P_i release of a particular subunit resulted in a change in the value of the corresponding element of the state vector. To further understand the importance of the cooperativity in the filament, the rate parameters via the results of the UCG model were uniformly scaled to probe the effect of increased or decreased cooperativity. The model was sampled using a Monte Carlo algorithm (see Supporting Materials and Methods for details).

RESULTS AND DISCUSSION

Multibody effects in kinetics of ATP hydrolysis and P_i release

The UCG model was used to study multibody effects in ATP hydrolysis and P_i release at the resolution of the MSM model. The hydrolysis of each actin subunit can be affected by several neighboring subunits. Ideally, one needs to consider all possible combinations of the nucleotide states of several neighboring units to study their effect on the rate of hydrolysis. To keep the number of such combinations tractable, we limited the study to a fairly small number of neighboring subunits by invoking the local nature of interactions between CG beads. The longest pairwise interactions in our model were between CG beads belonging to actin subunits that are two monomers apart in the filament. Hence, we limited our study of multibody effects to three neighboring subunits on each of the two sides of a given subunit, as described below.

For ATP hydrolysis, we designed a long UCG filament model consisting of 18,265 actin subunits (an integer number of copies of 13 subunits) as follows: we capped the barbed end of the filament with 26 ATP-bound subunits and the pointed end with 39 ATP-bound subunits to avoid any possible end effects. The remaining 18,200 subunits in the “bulk” of the filament were divided into sets of seven-subunit-long sections. The fourth subunit (marked subunit) in each section was an ATP-bound subunit, whereas three of its nearest neighbors toward the pointed end (1–3) and toward the barbed end (5–7) were randomly chosen to be either ATP-bound or ADP-P_i-bound subunits. In practice, the nucleotide states of the six neighbors of a marked subunit in each of the 2600 sections were randomly chosen from all $2^6 = 64$ possible combinations such that there were at least 40 copies of each combination in a single filament at random locations along its length. Only marked subunits were allowed to hydrolyze, whereas all the neighbors simply underwent Langevin dynamics and were constrained to remain in their initial nucleotide state. UCG simulations were run until all marked subunits hydrolyzed. These simulations were repeated 640 times, each with a unique filament design, and the conditional mean first passage time (MFPT) for each combination of neighboring states was calculated. The inverse of the MFPT for all the hydrolysis events provides the rate for that reaction in the UCG parametrized MSM when considering reactions at the full granularity of neighbors (76). At coarser resolutions, we refer to the corresponding effective rate as the average rate, given by rate $=$ MFPT^{-1}.

In the following, a unique six-digit "key" is used to denote a section with a particular combination of neighboring subunits. An unhydrolyzed ATP-bound subunit is represented as 0, and a hydrolyzed ADP-P_i-bound subunit is represented as 1. The key is simply the word formed by concatenating these representations, starting with the third nearest neighbor toward the pointed end and going through each consecutive neighbor up to the third nearest neighbor toward the barbed end.

Fig. 2 and Fig. S5 *a* show the variation in rate of ATP hydrolysis relative to the average rate as a function of certain representative combinations of states of neighboring subunits. The explicit dihedral angle dependence in Eqs. 2 and 4 was used, with $\eta = 0.125$. The ATP hydrolysis rate of a given subunit was found to vary by a maximum of about ±20% relative to its average rate depending on whether it was in an ATP-rich or an ADP-P_i-rich environment. The reaction rate was enhanced when all six neighboring subunits were in the unhydrolyzed ATP-bound state, whereas it was suppressed when all these neighbors were in the ADP-P_i-bound state. Similar variation in hydrolysis rate was observed even when ignoring the dependence of the two farthest neighbors (data corresponding to keys X0000X and X1111X in Fig. S5 *a*), supporting our assumption of the local nature of interactions. The observed variation was found to be insensitive to the explicit dihedral dependence (Fig. S5 *b*).

For P_i release, we designed long actin filaments similar to those used in the above simulations, and the barbed and pointed ends of the filaments were capped with ADP-P_i-bound subunits. The "bulk" of the filament was divided into seven-subunit-long sections, and each section was randomly chosen such that the fourth subunit was initially ADP-P_i bound and was allowed to release its P_i, whereas the rest of its six neighboring subunits mimicked all 64 possible combinations of states (either ADP-P_i or ADP bound) and were forced to remain in their initial state.

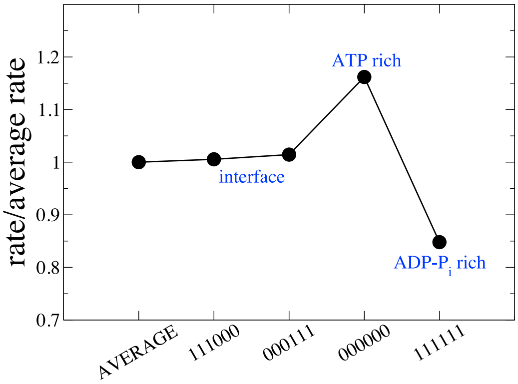

FIGURE 2 Multibody effect in ATP hydrolysis plotted as a ratio of the conditional rate with the average rate for specific combinations of nucleotide states of neighboring subunits. Combinations of neighboring subunit states are indicated using a key on the *x* axis that denotes the state (0 = unhydrolyzed, 1 = hydrolyzed) of each of the neighboring subunits, starting from the third neighbor toward the pointed end to the third neighbor toward the barbed end. Error bars indicate the standard error for each data point and are smaller than the symbol size for most of the data. To see this figure in color, go online. See Fig. S5 *b* for data corresponding to all 64 possible combinations.

The P_i release reaction rate was also affected by the state of neighboring subunits by a maximum of about ±20% over its average rate, as seen from Fig. 3 (also see Figs. S6 and S7). Note that the explicit dihedral angle dependence in Eqs. 2 and 4 was switched off in the P_i release reaction by setting $\eta = 0$. In contrast to ATP hydrolysis, the P_i release rate of a given subunit was enhanced when all of its

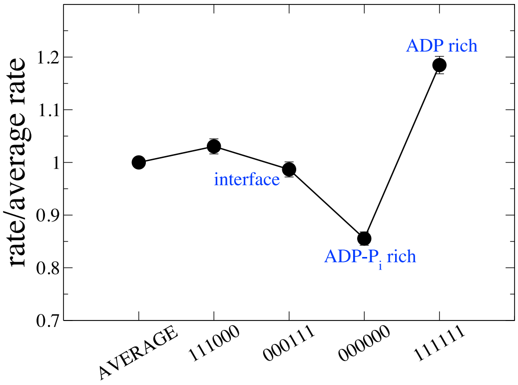

FIGURE 3 Multibody effect in P_i release plotted as a ratio of the conditional rate to the average rate for specific combinations of nucleotide states of neighboring subunits. The key on the *x* axis is similar to that described in Fig. 2 (except for the new definitions 0 = ADP-P_i, 1 = ADP). Error bars indicate the standard error for each data point. To see this figure in color, go online. See Fig. S7 for data corresponding to all 64 possible combinations.

neighbors were free of P_i. The rate was suppressed when all of its neighboring subunits were ADP-P_i bound. At the interface, where all three neighbors along the pointed end side of the marked subunit were ADP bound and those along the barbed end side of the marked subunit were ADP-P_i bound (corresponding to key 111000), the rate of reaction was only marginally higher relative to its average value. The observed variation was found to persist within a range of the chosen value for average acceptance probability (see Fig. S6).

Filament growth and role of multibody effects

The role of ATP hydrolysis and P_i release on filament growth has been previously studied using kinetic models that include polymerization and depolymerization of subunits at the ends of the filament, along with ATP hydrolysis in subunits belonging to the filament (34,35,47). These models have been shown to agree well with experimental data in terms of the average filament growth rate, independent of whether the vectorial (35) or stochastic (34) mechanism of hydrolysis and/or P_i release is assumed. In these models, multibody effects were ignored to keep the models tractable and possibly because of lack of any evidence suggesting such effects. On the other hand, our UCG model predicted a strong multibody effect, manifested through a significant variation in both the ATP hydrolysis and the P_i release kinetics depending on the state of neighboring subunits.

In the following, we tested the implications of the cooperativity predicted by our UCG model. This was performed by extending the previous MSM characterizing only hydrolysis via the addition of states and transitions representing polymerization and depolymerization. As described below, the primary distinguishing feature of our MSM with respect to existing kinetic models was the explicit dependence of rates of ATP hydrolysis and P_i release on the nucleotide states of neighboring subunits, based on the predictions of our UCG model (Figs. S5 *b* and S7).

We chose to study the implication of this cooperativity by modifying two representative models reported in (34,47) as follows: 1) in (34), the filament growth kinetics at a constant free actin concentration was studied by assuming a random mechanism of ATP hydrolysis and P_i release, and the resulting constant average filament growth rate was reported. For direct comparison, we modified their model to include the cooperativity in ATP hydrolysis and P_i release while keeping the rest of the model unmodified. 2) Filament growth kinetics in a conserved system was studied in (47), in which the total mass of actin was assumed to be constant such that at steady state, the average filament length remained constant. ATP and ADP-Pi were made indistinguishable in their model by assuming fast ATP hydrolysis. To enable a direct comparison, we only modified their model at places involving random P_i release to include our predicted cooperativity in P_i release while keeping the rest of the model unmodified.

The filament was initialized with n_0 subunits and was assumed to be in a solution of free monomeric subunits at a specified concentration. Addition of a free ATP-bound subunit at the barbed end of the filament increased the filament length, whereas dissociation of the terminal subunit (ATP or ADP-P_i or ADP bound) at the barbed or pointed ends decreased its length. The rest of the subunits belonging to the filament underwent ATP hydrolysis and/or P_i release as in the original models in (34,47). The macroscopic rate constants for these reactions are given in Table 1 and were chosen to be same as in the original models with which we compared our predictions.

The model was sampled using a Monte Carlo (MC) algorithm to study evolution of the filament, keeping track of the location of all the actin subunits in the filament. For each set of parameters, 1000 statistically independent simulations were run. Details of the MC algorithm are provided in the Supporting Materials and Methods.

Filament dynamics at constant free actin concentration

In (34), the total free actin concentration was assumed to be constant. This mimics experimental conditions in which, for example, a solution of G-actin at constant concentration is flowing through the system using microfluidic devices. Because the total concentration of free actin does not change with time, the resulting filament either grows with time if the free actin concentration is above the critical concentration or shrinks with time if the concentration is lower than the critical concentration.

The filament growth rates at different free actin concentrations obtained in experiments have been shown to be in agreement with either the vectorial or stochastic mechanisms of hydrolysis (34,35,47). We modified our MSM based on the kinetic model in (34) by using corresponding parameters from the first row of Table 1. For direct

TABLE 1 Macroscopic Rate Constants Used in the Kinetic Models

	$K_{pol.}$ ($\mu M^{-1}s^{-1}$)		$K_{dis., barbed}$ (s^{-1})			$K_{dis., pointed}$ (s^{-1})			
Model reference	barbed	pointed	ATP	ADP-P_i	ADP	ATP	ADP	$K_{hyd.}$ (s^{-1})	$K_{rel.}$ (s^{-1})
(34)	11.6	–	1.4	1.1	7.2	–	–	0.3 (34)	0.004
(47)	11.6	–	1.4	–	7.2	0.8	0.27	–	0.003

$K_{pol.}$ is the polymerization rate constant, $K_{dis., barbed}$ is the depolymerization rate constant at the barbed end, and $K_{dis., pointed}$ is that at the pointed end. $K_{hyd.}$ and $K_{rel.}$ are rate constants of ATP hydrolysis and P_i release, respectively.

comparison with (34), we included all three possible bound nucleotide states of subunits in our model: ATP, ADP-P_i, and ADP. Additionally, we assumed that no polymerization or dissociation took place at the pointed end, similar to the original model in (34). Thus, the model consisted of polymerization and dissociation at the barbed end, with ATP hydrolysis and P_i release throughout the filament, and hence was identical to the model in (34). We then modified the model to incorporate the multibody effects observed in our UCG simulations by modulating the ATP hydrolysis and P_i release rates using the data in Figs. 2 and 3 (and Figs. S5 *b* and S7) as follows. Our MC algorithm was designed to keep track of the states of all actin subunits in the filament. This allowed us to use all of the data in Figs. S5 *b* and S7 because we knew the instantaneous nucleotide state of neighbors of each actin subunit.

We introduced a parameter X in the model, as discussed below, to have the ability to interpolate between a purely stochastic mechanism ($X = 0$) and the UCG predictions ($X = 1$). Because the multibody effects predicted by our UCG model were sensitive to the UCG parameters (although similar in trends; see Figs. S5 *a* and S6), the parameter X also allowed us to extrapolate beyond the UCG model predictions specific to the choice of UCG parameters in our final model. Given a state of neighboring subunits with a corresponding key, the net rate of ATP hydrolysis is defined as

$$K_{\text{hyd.}}^{\text{net}}(\text{key}) = K_{\text{hyd.}}[1 + X\varDelta K(\text{key})], \tag{5}$$

where

$$\varDelta K(\text{key}) = \frac{K}{K_{\text{hyd.}}}(\text{key}) - 1. \tag{6}$$

Here, the first term on the right-hand side of Eq. 6 is the ratio of conditional rate of ATP hydrolysis K for a combination of states of neighboring subunits specified with key, to the average rate of ATP hydrolysis $K_{\text{hyd.}}$ for all such possible combinations (same quantity as the y axis in Figs. 2 and S5 *b*). For example, the ratio $K/K_{\text{hyd.}}$ (key $= 000000) \approx 1.16$ for a subunit surrounded by all ATP-bound neighbors. The rate of ATP hydrolysis for each ATP-bound subunit was similarly modulated by using in Eq. 6 the ratio $K/K_{\text{rel.}}$ from Fig. S5 *b* corresponding to its instantaneous key at each MC step. When an ATP-bound subunit hydrolyzed during an MC step with an ATP hydrolysis rate governed by the instantaneous nucleotide state of its neighbors, the keys of all its neighboring subunits were updated at the end of the step, which in turn modulated the ATP hydrolysis rates of its neighboring ATP-bound subunits in all future MC steps.

The multibody rate of P_i release, $K_{\text{rel.}}^{\text{net}}$, was similarly defined as follows to take into account the variation with state of neighbors:

$$K_{\text{rel.}}^{\text{net}}(\text{key}) = K_{\text{rel.}}[1 + X\varDelta K(\text{key})], \tag{7}$$

where

$$\varDelta K(\text{key}) = \frac{K}{K_{\text{rel.}}}(\text{key}) - 1. \tag{8}$$

The first term of the right-hand side of Eq. 8 is the ratio of conditional rate of P_i release K for a combination of states of neighboring subunits specified with the key, to the average rate of P_i release $K_{\text{rel.}}$ for all such possible combinations (same quantity as the y axis in Figs. 3 and S7). For example, the ratio $K/K_{\text{rel.}}$ (key $= 111111) \approx 1.18$ for a subunit surrounded by all ADP-bound neighbors, as observed from Fig. 3. The rate of P_i release for each ADP-P_i-bound subunit was similarly modulated by using in Eq. 8 the ratio $K/K_{\text{rel.}}$ from Fig. S7 corresponding to its instantaneous key at each MC step. When a ADP-P_i-bound subunit released its P_i during an MC step with a P_i release rate governed by the instantaneous nucleotide state of its neighbors, the keys of all its neighboring subunits were updated at the end of the step, which in turn modulated the P_i release rates of its neighboring ADP-P_i-bound subunits in all future MC steps.

The free actin subunits were implicitly present at a constant concentration c. The filament initially consisted of n_0 subunits, with a two-third fraction of the filament near the pointed end being ADP bound and the reminder tip near the barbed end made of ATP-bound subunits.

Fig. 4 *a* shows the mean total filament length (number of subunits) obtained from 1000 statistical runs for two different free actin concentrations. The left panel corresponds to a free actin concentration below the critical concentration. The filament, initially made of $n_0 = 2000$ subunits, shrunk at a constant rate as subunits dissociated. The right panel corresponds to a free actin concentration above the critical concentration. The filament, initially made of $n_0 = 1000$ subunits, grew at a constant rate. For both concentrations, the filament growth followed a different trajectory depending on the strength of multibody effects incorporated into the model.

The slope of the filament length curves, ignoring the initial transient (see Fig. S9), gives the growth rate of the filament. Fig. 4 *b* shows the growth rate of the filament as a function of the free actin concentration. It is evident that the filament growth rate is not dramatically affected by absence ($X = 0$) or presence ($X \neq 0$) of the multibody effects. Note that small differences in the growth rate can affect the filament length trajectories significantly, especially at longer times. Near the critical concentration, at which the growth rate is zero, the strength of multibody effects incorporated in the model affected the growth rate significantly, as the inset of Fig. 4 *b* shows. However, the absolute growth rate near the critical concentration was too low to make these variations significant.

Although the filament growth kinetics were not affected significantly by the mechanism of hydrolysis and P_i release,

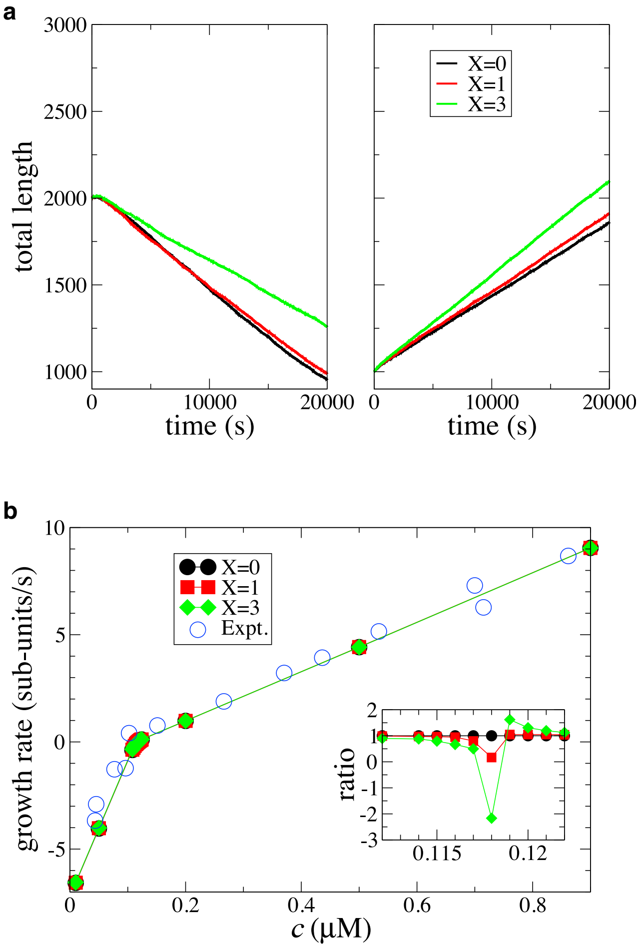

FIGURE 4 (*a*) Filament length dynamics for different strengths of multibody effect shown in different colors at concentrations below (*left panel*, $c = 0.116\ \mu$M) and above (*right panel*, $c = 0.120\ \mu$M) the critical concentration. (*b*) Filament growth rate (*filled symbols*) as a function of concentration of free actin is shown. Different colors represent different strengths of multibody effects. Open circles are experimental data taken from (34), originally extracted from experiments in (47). The inset shows the ratio of growth rate at a given strength of multibody effects compared to the growth rate at $X = 0$. To see this figure in color, go online.

the composition of the filaments changed significantly as multibody effects were made stronger in the model. As the filament grew at a constant rate above the critical concentration, more and more ATP subunits were added to its barbed end. These subunits then underwent hydrolysis and P_i release. As the model ignored any dissociation at the pointed end, the number of ADP subunits also grew with time. On the other hand, the number of ADP-P_i subunits remained nearly constant after an initial transient. Fig. 5 *a* shows the average length of a contiguous ADP-P_i section for a range of free actin concentrations obtained as a mean over the nearly constant regime and over 1000 simulation runs. At a given free actin concentration, the average length increased with increasing strength of multibody effects. This trend was also reflected in the mean value of maximal length of a contiguous ADP-P_i section shown in Fig. 5 *b*.

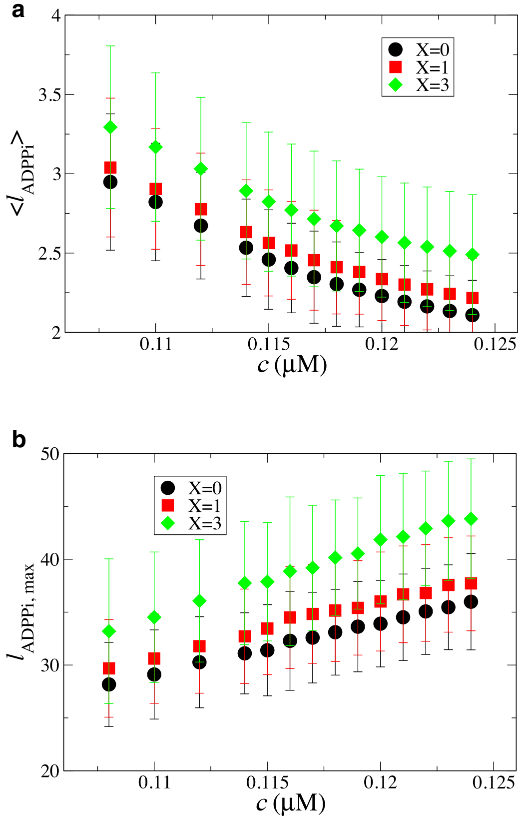

FIGURE 5 Variation in filament composition due to incorporation of multibody effects in ATP hydrolysis and P_i release shown in terms of (*a*) the average length of a contiguous ADP-P_i section along the filament and (*b*) maximal length of a contiguous ADP-P_i section along the filament. Different symbols indicate varying strengths of multibody effects, as indicated in the legend. To see this figure in color, go online.

When the free actin concentration is kept constant, the filament is either growing or shrinking at a constant rate with time except at the critical concentration, for which the growth rate is zero. Because there is no steady state with constant filament length in this system (except at critical concentration), we listed 90 unique compositions for an arbitrarily chosen filament length of 325 subunits based on MC runs of the system at $c_0 = 0.120\ \mu$M (just above the critical concentration; see Fig. 4 *b*) to calculate the persistence length. The average persistence length for a filament length of 325 subunits for the random mechanism corresponding to $X = 0$ cooperativity was found to be 14.2 ($\pm$ 0.2) μm, whereas that for $X = 3$ cooperativity was found to be 14.4 ($\pm$ 0.2) μm.

Filament dynamics in a conserved system

A conserved system (in which the total number of subunits in the system, including free monomers and polymerized subunits, remains constant in time) was proposed in (47) to study the effect of vectorial versus stochastic hydrolysis on the transient part (see Fig. 6) of filament growth. For

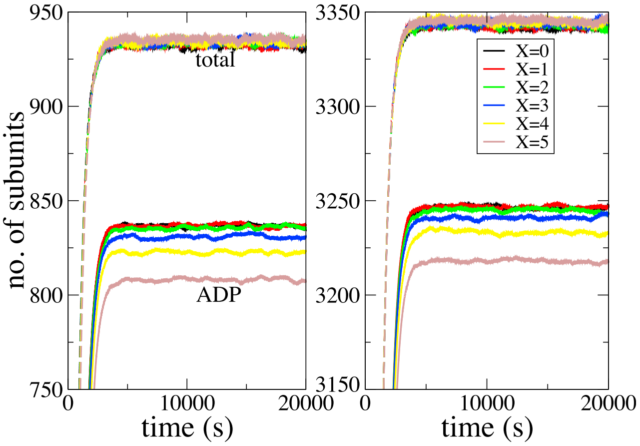

FIGURE 6 The total number of subunits (*dotted lines*) and the number of hydrolyzed subunits (*solid lines*) in the filament as a function of simulation time. Different colors correspond to varying strengths of multibody effects incorporated in the model, with $X = 0$ corresponding to a purely stochastic hydrolysis. The left panel corresponds to $c_0 = 0.3$ μM, and the right panel corresponds to $c_0 = 0.7$ μM. To see this figure in color, go online.

the conserved system, starting with an initial filament of a certain length and an initial free monomer concentration c_0 that is above the critical concentration at which the net filament growth rate is positive, the free monomer concentration keeps on dropping as the filament grows, thereby reducing the polymerization rate. This continues until the concentration is just enough to balance the net polymerization and dissociation rates, resulting in a nearly steady filament length at larger times. It was predicted that although the vectorial and random mechanisms would result in a similar steady filament length, the transient from the initial filament to the steady filament would show significant variation depending on the mechanism of hydrolysis and P_i release. For a direct comparison with (47), we further modified our model such that the phenomenology between the two models was exactly the same. Firstly, ATP hydrolysis was assumed to be fast relative to P_i release, identical to the model in (47). Hence, ATP and ADP-P_i were made indistinguishable in the model, as done in (47). Further, the filament was allowed to polymerize only at the barbed end. The resulting model consisted of only two states of the nucleotide bound to actin subunits in the filament: ATP and ADP. Note that we used the notation ATP to be consistent with (47), although it equivalently corresponds to the bound nucleotide state ADP-P_i and undergoes P_i release reaction, resulting in the nucleotide state ADP. The rate constants in the second row of Table 1 corresponding to (47) were used.

To incorporate the multibody effects as revealed in the UCG simulations into the model, an additional modification was made. The multibody rate of P_i release, $K_{\mathrm{rel.}}^{\mathrm{net}}$, was defined using Eq. 7 to take into account the variation with state of neighbors. Similar to the preceding section, the rate of P_i release for each ATP (= ADP-P_i)-bound subunit was modulated by using in Eq. 8 the ratio $K/K_{\mathrm{rel.}}$ from Fig. S7 corresponding to its instantaneous key at each MC step. When an ATP-bound subunit released its P_i during an MC step with a P_i release rate governed by the instantaneous nucleotide state of its neighbors, the keys of all its neighboring subunits were updated at the end of the step, which in turn modulated the P_i release rates of its neighboring ATP-bound subunits in all future MC steps. As mentioned earlier, the parameter X was used to vary the strength of multibody effects in the model. The specific values implied by the UCG parameters chosen in this work corresponded to $X = 1$. However, acknowledging the possibility of other choices for the UCG parameters, we allowed X to vary up to $X = 5$ (because $K_{\mathrm{rel.}}^{\mathrm{net}}(\text{key} = 000000) < 0$ for $X = 6$ and beyond).

Fig. 6 shows the multibody effect on mean filament dynamics observed across 1000 simulation runs for two values of initial concentration c_0. The number of hydrolyzed subunits, initially set to four, underwent a transient, beyond which it remained nearly constant. Although the qualitative features were similar across all strengths of multibody effects studied, there was an increasing delay in hydrolysis relative to the filament growth dynamics as this strength increased. Moreover, the asymptotic value of hydrolyzed subunits systematically decreased. The total number of subunits and hence the filament length remained nearly constant after undergoing a transient from its initial value of six. However, both the transient and the asymptotic value of the filament length were not found to be sensitive to the strength of multibody effects.

On the other hand, the filament composition showed a stronger dependence on the mechanism of P_i release. A contiguous ATP section, throughout which all the consecutive subunits were ATP bound, could easily be identified in our simulations. At every instant, we identified the number and length of these sections in the filament and calculated their mean values across all 1000 simulation runs. Fig. 7 *a* shows the average length of a contiguous ATP section as a function of time. In comparison to a purely random P_i release, the multibody cooperative effects predicted much longer contiguous ATP sections. The same trend was also observed in the mean of the maximal length of these sections across each simulation run, as shown in Fig. 7 *b*.

For systematic comparison of persistence length with the previous section, we chose an initial actin concentration $c_0 = 0.2$ μM that gave a filament of average length 325 subunits. We listed ~90 unique compositions that the filament of length 325 subunits exhibited and calculated the average persistence length based on these compositions. The average persistence length of the filament under these conditions was found to be 13.5 (± 0.2) μm for the random mechanism corresponding to $X = 0$ cooperativity, 13.6 (± 0.2) μm for $X = 3$ cooperativity, and 13.9 (± 0.2) μm for $X = 5$ cooperativity.

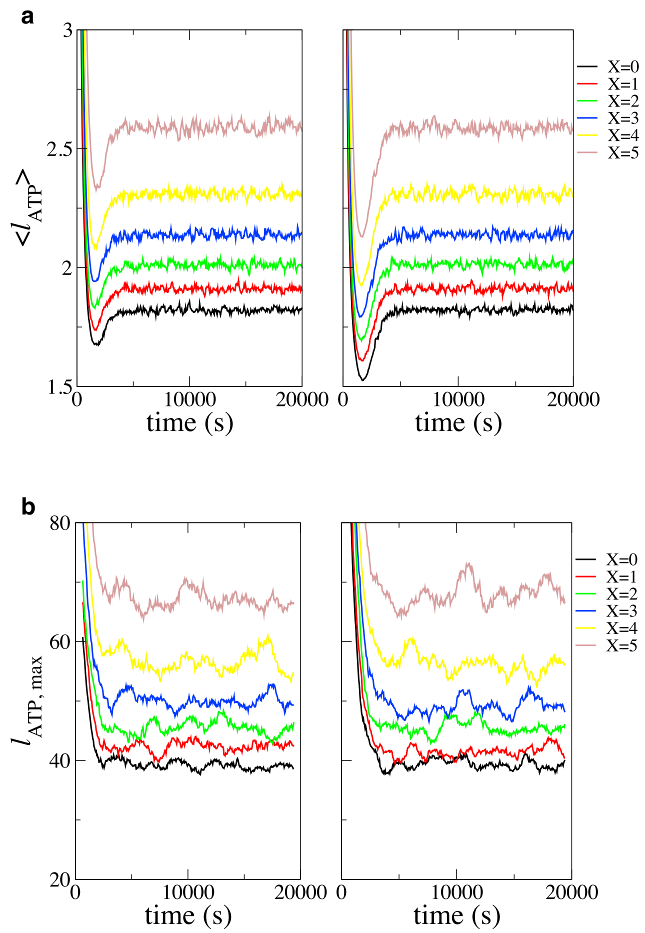

FIGURE 7 Variation in filament composition due to incorporation of multibody effects in P_i release reaction shown as (*a*) average length of a contiguous ATP section along the filament and (*b*) maximal length of a contiguous ATP section along the filament. Different colors indicate varying strengths of multibody effects, as indicated in the legend. The left panel corresponds to $c_0 = 0.3$ μM, and the right panel corresponds to $c_0 = 0.7$ μM. To see this figure in color, go online.

CONCLUSIONS

Two classes of kinetic models have been proposed for actin filaments based on the mechanism of hydrolysis of ATP and the subsequent release of P_i. The random hydrolysis mechanism (2,34,42,46) assumes an equal probability of ATP hydrolysis and P_i release at every position in the filament. On the other extreme, the vectorial model (8,35,43,45) assumes that hydrolysis can take place only at the boundary between the unhydrolyzed and hydrolyzed parts of the filament. Although the two models fundamentally differ in terms of hydrolysis, the difference seems to be insignificant for filament dynamics, especially in terms of the filament growth rate that is typically measured in experiments.

The random hydrolysis mechanism assumes no cooperativity in hydrolysis, so that subunits at any position along the filament hydrolyze at the same rate at all times. The vectorial mechanism assumes maximal cooperativity in hydrolysis such that only those subunits that are at the interface between unhydrolyzed and hydrolyzed units undergo hydrolysis at a nonzero rate and all other subunits throughout the filament effectively have a zero rate of hydrolysis. Our UCG and kinetic models allowed us to explore the possibility of intermediate levels of cooperativity, in which the nearby neighbors affect the rate of hydrolysis of a given subunit in a filament.

More specifically, the UCG model predicted a substantial variation in the rates of hydrolysis and P_i release. The rate of ATP hydrolysis was enhanced by ~20% when an ATP actin subunit was in an ATP-rich environment and decreases by ~20% when in an ADP-P_i-rich environment. In the scenario of a growing actin filament, such a variation implies that the filament would be more fragmented in ATP in comparison to random hydrolysis because subunits in the ATP-rich region will hydrolyze faster to form ADP-P_i, which then slows down the hydrolysis of nearby neighbors to a certain extent. Data from our kinetic model reflected this in terms of the average and maximal lengths of ATP sections (data not shown). In contrast, the rate of P_i release from an ADP-P_i subunit was suppressed when it was in an ADP-P_i-rich environment and enhanced by about ~20% when in an ADP-rich environment. This implies that in a growing filament, the filament would be less fragmented in ADP-P_i in comparison to random hydrolysis because subunits in the ADP-P_i-rich region of the filament will release their P_i slower to form ADP, which will then accelerate the P_i release of neighboring subunits to a certain extent. This is exactly what we observed in our kinetic model, as shown by the data in Fig. 5.

Our predictions imply that there is substantial cooperativity in ATP hydrolysis and P_i release reactions, characterized by a variation of about ±20% in the rates of these reactions relative to the corresponding average rates, and hence provide evidence for a significant deviation from a random mechanism in each of these reactions. Further, we observe that the cooperativity extends beyond the nearest neighbors. On the other hand, the rate of ATP hydrolysis at the ATP/ADP-P_i interface is not different from the average rate of ATP hydrolysis in the filament, characterized by a variation within ±1.5% relative to the average rate (Fig. 2). The same is true for the P_i release reaction (Fig. 3), in which the rate of P_i release at the interface is approximately the same as the average rate of P_i release in the filament, characterized by a variation within ±3% relative to the average rate. This is in contrast with the prediction of a strong cooperativity and the resulting implication of an enhancement in rate of P_i release at the interface by a factor of 10^6–10^8 relative to the average rate made in (44), although their analysis ignored any multibody effects beyond a simpler nearest-neighbor cooperativity (44,48,49). Clearly, the nature of our predicted cooperativity does not show any signs in support of a purely vectorial ATP hydrolysis or P_i release. A detailed comparison of our model with available experimental data is beyond the scope of this work and is left to be studied in the future.

An important point to consider is that the hydrolysis reaction is faster than the P_i release reaction by about two orders of magnitude (Table 1). Although the relative variation in rates of hydrolysis and P_i release are of the same extent in Figs. 2 and 3, the variation in absolute rate of the faster hydrolysis reaction is expected to play an insignificant role in filament dynamics and composition. The slower P_i release reaction is the rate-determining step and hence should have the strongest effect on filament dynamics and composition.

Although the filament composition changes significantly with the cooperativity in ATP hydrolysis and P_i release, long-length-scale filament properties such as the persistence length do not reflect this change to a measurable extent. As seen from Fig. 6, in a conserved system, a steady state characterized by a filament length that fluctuates around a constant average value was reached as the actin monomer concentration approached the treadmilling concentration. The average persistence length of the filament under these conditions was found to be approximately identical between random and cooperative mechanisms. When the free actin concentration was kept constant, the persistence length for 90 representative compositions of identical filament lengths was also found to exhibit a weak dependence on the mechanism of hydrolysis. The changes in persistence length corresponding to the changes in composition were expected to be small, given the narrow range between persistence lengths for a pure ATP filament, a pure ADP-P_i filament, and a pure ADP filament (Fig. S1).

In conclusion, our bottom-up CG strategy enabled us to probe the cooperative nature of ATP hydrolysis and P_i release in F-actin in detail. We found that the mechanism of these reactions is not fully random but does depend on the state of neighboring subunits. Although the vectorial model is a reasonable attempt made at simplifying a more accurate but complicated cooperativity such as the one we observe in this work, we did not find any evidence supporting the extent of variation in rates as is suggested by a purely vectorial model.

Our UCG model provides a framework to investigate many important problems related to ATP hydrolysis in actin. Several actin binding proteins (e.g., cofilin (77)) have affinities that depend on the state of the bound nucleotide. In recent work (60), a bottom-up mesoscale modeling approach based on atomistic simulations was used to simulate different modes of applying strain in actin filaments and to study the resulting effect on the binding and activity of the actin binding protein cofilin. Our model can be used to further investigate the implications of applying strain in actin filaments on the hydrolysis of the bound nucleotide and the resulting combined effect of strain and nucleotide state on binding of actin-binding proteins.

SUPPORTING MATERIAL

Supporting Materials and Methods and nine figures are available at http://www.biophysj.org/biophysj/supplemental/S0006-3495(18)31011-7.

AUTHOR CONTRIBUTIONS

H.H.K., A.D., and G.M.H. contributed to simulation design and analysis. H.H.K. and A.D. designed simulation code. H.H.K., A.E.P.D., and A.D. designed parameter optimization algorithms. G.A.V. designed research. A.C.S. and E.M.D.L.C. provided crucial biological insights. H.H.K., A.E.P.D., and G.M.H. drafted the manuscript.

ACKNOWLEDGMENTS

This research was supported in part by the National Science Foundation (NSF) through NSF grant CHE-1465248 and in part by the Department of Defense Army Research Office through Multidisciplinary University Research Initiative grant W911NF1410403. The computations in this work used the Extreme Science and Engineering Discovery Environment, which is supported by NSF grant number ACI-1548562. Additional computational resources were provided by the Research Computing Center at The University of Chicago. G.M.H. was supported by a Ruth L. Kirschstein National Research Service Award (National Institute of General Medical Sciences, F32 GM11345-01). A.E.P.D. acknowledges support by the Department of Defense through the National Defense Science & Engineering Graduate Fellowship Program. E.M.D.L.C. and A.C.S. were supported by the National Institutes of Health through grant R01-GM097348.

REFERENCES

1. Kabsch, W., H. G. Mannherz, ..., K. C. Holmes. 1990. Atomic structure of the actin:DNase I complex. *Nature.* 347:37–44.
2. Blanchoin, L., and T. D. Pollard. 2002. Hydrolysis of ATP by polymerized actin depends on the bound divalent cation but not profilin. *Biochemistry.* 41:597–602.
3. Rould, M. A., Q. Wan, ..., K. M. Trybus. 2006. Crystal structures of expressed non-polymerizable monomeric actin in the ADP and ATP states. *J. Biol. Chem.* 281:31909–31919.
4. Saunders, M. G., and G. A. Voth. 2011. Water molecules in the nucleotide binding cleft of actin: effects on subunit conformation and implications for ATP hydrolysis. *J. Mol. Biol.* 413:279–291.
5. McCullagh, M., M. G. Saunders, and G. A. Voth. 2014. Unraveling the mystery of ATP hydrolysis in actin filaments. *J. Am. Chem. Soc.* 136:13053–13058.
6. Sun, R., O. Sode, ..., G. A. Voth. 2017. Simulating protein mediated hydrolysis of ATP and other nucleoside triphosphates by combining QM/MM molecular dynamics with advances in metadynamics. *J. Chem. Theory Comput.* 13:2332–2341.
7. Pollard, T. D. 1986. Rate constants for the reactions of ATP- and ADP-actin with the ends of actin filaments. *J. Cell Biol.* 103:2747–2754.
8. Carlier, M. F., D. Pantaloni, and E. D. Korn. 1987. The mechanisms of ATP hydrolysis accompanying the polymerization of Mg-actin and Ca-actin. *J. Biol. Chem.* 262:3052–3059.
9. Wegner, A. 1977. The mechanism of ATP hydrolysis by polymer actin. *Biophys. Chem.* 7:51–58.
10. Brenner, S. L., and E. D. Korn. 1984. Evidence that F-actin can hydrolyze ATP independent of monomer-polymer end interactions. *J. Biol. Chem.* 259:1441–1446.
11. Pollard, T. D., and A. G. Weeds. 1984. The rate constant for ATP hydrolysis by polymerized actin. *FEBS Lett.* 170:94–98.

12. Carlier, M., D. Pantaloni, and E. Korn. 1986. The effects of Mg2+ at the high-affinity and low-affinity sites on the polymerization of actin and associated ATP hydrolysis. *J. Biol. Chem.* 261:785–792.
13. Carlier, M. F., and D. Pantaloni. 1986. Direct evidence for ADP-Pi-F-actin as the major intermediate in ATP-actin polymerization. Rate of dissociation of Pi from actin filaments. *Biochemistry.* 25:7789–7792.
14. Carlier, M. F. 1987. Measurement of Pi dissociation from actin filaments following ATP hydrolysis using a linked enzyme assay. *Biochem. Biophys. Res. Commun.* 143:1069–1075.
15. Carlier, M. F., D. Pantaloni, …, M. R. Webb. 1988. The hydrolysis of ATP that accompanies actin polymerization is essentially irreversible. *FEBS Lett.* 235:211–214.
16. Carlier, M. F., and D. Pantaloni. 1988. Binding of phosphate to F-ADP-actin and role of F-ADP-Pi-actin in ATP-actin polymerization. *J. Biol. Chem.* 263:817–825.
17. Melki, R., S. Fievez, and M. F. Carlier. 1996. Continuous monitoring of Pi release following nucleotide hydrolysis in actin or tubulin assembly using 2-amino-6-mercapto-7-methylpurine ribonucleoside and purine-nucleoside phosphorylase as an enzyme-linked assay. *Biochemistry.* 35:12038–12045.
18. Orlova, A., and E. H. Egelman. 1992. Structural basis for the destabilization of F-actin by phosphate release following ATP hydrolysis. *J. Mol. Biol.* 227:1043–1053.
19. Kang, H., M. J. Bradley, …, E. M. De La Cruz. 2012. Identification of cation-binding sites on actin that drive polymerization and modulate bending stiffness. *Proc. Natl. Acad. Sci. USA.* 109:16923–16927.
20. Kang, H., M. J. Bradley, …, E. M. De La Cruz. 2013. Regulation of actin by ion-linked equilibria. *Biophys. J.* 105:2621–2628.
21. Hocky, G. M., J. L. Baker, …, G. A. Voth. 2016. Cations stiffen actin filaments by adhering a key structural element to adjacent subunits. *J. Phys. Chem. B.* 120:4558–4567.
22. Isambert, H., P. Venier, …, M. F. Carlier. 1995. Flexibility of actin filaments derived from thermal fluctuations. Effect of bound nucleotide, phalloidin, and muscle regulatory proteins. *J. Biol. Chem.* 270:11437–11444.
23. Mehrafrooz, B., and A. Shamloo. 2018. Mechanical differences between ATP and ADP actin states: a molecular dynamics study. *J. Theor. Biol.* 448:94–103.
24. Yogurtcu, O. N., J. S. Kim, and S. X. Sun. 2012. A mechanochemical model of actin filaments. *Biophys. J.* 103:719–727.
25. Bidone, T. C., T. Kim, …, R. D. Kamm. 2015. Multiscale impact of nucleotides and cations on the conformational equilibrium, elasticity and rheology of actin filaments and crosslinked networks. *Biomech. Model. Mechanobiol.* 14:1143–1155.
26. Lyman, E., J. Pfaendtner, and G. A. Voth. 2008. Systematic multiscale parameterization of heterogeneous elastic network models of proteins. *Biophys. J.* 95:4183–4192.
27. Chu, J. W., and G. A. Voth. 2006. Coarse-grained modeling of the actin filament derived from atomistic-scale simulations. *Biophys. J.* 90: 1572–1582.
28. Fan, J., M. G. Saunders, and G. A. Voth. 2012. Coarse-graining provides insights on the essential nature of heterogeneity in actin filaments. *Biophys. J.* 103:1334–1342.
29. Saunders, M. G., and G. A. Voth. 2012. Comparison between actin filament models: coarse-graining reveals essential differences. *Structure.* 20:641–653.
30. Prinz, J. H., H. Wu, …, F. Noé. 2011. Markov models of molecular kinetics: generation and validation. *J. Chem. Phys.* 134:174105.
31. Bowman, G. R., V. Pande, and F. Noe. 2014. An Introduction to Markov State Models and Their Application to Long Timescale Molecular Simulation. Springer, Dordrecht, The Netherlands.
32. Chodera, J. D., and F. Noé. 2014. Markov state models of biomolecular conformational dynamics. *Curr. Opin. Struct. Biol.* 25:135–144.
33. Nuske, F., H. Wu, …, F. Noe. 2017. Markov state models from short non-equilibrium simulations-analysis and correction of estimation bias. *J. Chem. Phys.* 146:094104.
34. Vavylonis, D., Q. Yang, and B. O'Shaughnessy. 2005. Actin polymerization kinetics, cap structure, and fluctuations. *Proc. Natl. Acad. Sci. USA.* 102:8543–8548.
35. Stukalin, E. B., and A. B. Kolomeisky. 2006. ATP hydrolysis stimulates large length fluctuations in single actin filaments. *Biophys. J.* 90:2673–2685.
36. Dama, J. F., A. V. Sinitskiy, …, G. A. Voth. 2013. The theory of ultra-coarse-graining. 1. General principles. *J. Chem. Theory Comput.* 9:2466–2480.
37. Davtyan, A., J. F. Dama, …, G. A. Voth. 2014. The theory of ultra-coarse-graining. 2. Numerical implementation. *J. Chem. Theory Comput.* 10:5265–5275.
38. Dama, J. F., J. Jin, and G. A. Voth. 2017. The theory of ultra-coarse-graining. 3. Coarse-grained sites with rapid local equilibrium of internal states. *J. Chem. Theory Comput.* 13:1010–1022.
39. Jin, J., and G. A. Voth. 2018. Ultra-coarse-grained models allow for an accurate and transferable treatment of interfacial systems. *J. Chem. Theory Comput.* 14:2180–2197.
40. Fujiwara, I., D. Vavylonis, and T. D. Pollard. 2007. Polymerization kinetics of ADP- and ADP-Pi-actin determined by fluorescence microscopy. *Proc. Natl. Acad. Sci. USA.* 104:8827–8832.
41. Jégou, A., T. Niedermayer, …, G. Romet-Lemonne. 2011. Individual actin filaments in a microfluidic flow reveal the mechanism of ATP hydrolysis and give insight into the properties of profilin. *PLoS Biol.* 9:e1001161.
42. Pieper, U., and A. Wegner. 1996. The end of a polymerizing actin filament contains numerous ATP-subunit segments that are disconnected by ADP-subunits resulting from ATP hydrolysis. *Biochemistry.* 35:4396–4402.
43. Pantaloni, D., T. L. Hill, …, E. D. Korn. 1985. A model for actin polymerization and the kinetic effects of ATP hydrolysis. *Proc. Natl. Acad. Sci. USA.* 82:7207–7211.
44. Burnett, M. M., and A. E. Carlsson. 2012. Quantitative analysis of approaches to measure cooperative phosphate release in polymerized actin. *Biophys. J.* 103:2369–2378.
45. Korn, E. D., M. F. Carlier, and D. Pantaloni. 1987. Actin polymerization and ATP hydrolysis. *Science.* 238:638–644.
46. Ohm, T., and A. Wegner. 1994. Mechanism of ATP hydrolysis by polymeric actin. *Biochim. Biophys. Acta.* 1208:8–14.
47. Ranjith, P., K. Mallick, …, D. Lacoste. 2010. Role of ATP-hydrolysis in the dynamics of a single actin filament. *Biophys. J.* 98:1418–1427.
48. Jégou, A., T. Niedermayer, …, G. Romet-Lemonne. 2013. On phosphate release in actin filaments. *Biophys. J.* 104:2778–2779.
49. Burnett, M. M., and A. E. Carlsson. 2013. Response to "on phosphate release in actin filaments". *Biophys. J.* 104:2780.
50. Mackerell, A. D., Jr., M. Feig, and C. L. Brooks, III. 2004. Extending the treatment of backbone energetics in protein force fields: limitations of gas-phase quantum mechanics in reproducing protein conformational distributions in molecular dynamics simulations. *J. Comput. Chem.* 25:1400–1415.
51. Humphrey, W., A. Dalke, and K. Schulten. 1996. VMD: visual molecular dynamics. *J. Mol. Graph.* 14:33–38, 27–28.
52. Phillips, J. C., R. Braun, …, K. Schulten. 2005. Scalable molecular dynamics with NAMD. *J. Comput. Chem.* 26:1781–1802.
53. Van Der Spoel, D., E. Lindahl, …, H. J. Berendsen. 2005. GROMACS: fast, flexible, and free. *J. Comput. Chem.* 26:1701–1718.
54. Bussi, G., D. Donadio, and M. Parrinello. 2007. Canonical sampling through velocity rescaling. *J. Chem. Phys.* 126:014101.
55. Oda, T., M. Iwasa, …, A. Narita. 2009. The nature of the globular- to fibrous-actin transition. *Nature.* 457:441–445.
56. Pfaendtner, J., D. Branduardi, …, G. A. Voth. 2009. Nucleotide-dependent conformational states of actin. *Proc. Natl. Acad. Sci. USA.* 106:12723–12728.
57. Saunders, M. G., J. Tempkin, …, G. A. Voth. 2014. Nucleotide regulation of the structure and dynamics of G-actin. *Biophys. J.* 106:1710–1720.

58. McCullough, B. R., L. Blanchoin, …, E. M. De la Cruz. 2008. Cofilin increases the bending flexibility of actin filaments: implications for severing and cell mechanics. *J. Mol. Biol.* 381:550–558.

59. Pfaendtner, J., E. Lyman, …, G. A. Voth. 2010. Structure and dynamics of the actin filament. *J. Mol. Biol.* 396:252–263.

60. Schramm, A. C., G. M. Hocky, …, E. M. De La Cruz. 2017. Actin filament strain promotes severing and cofilin dissociation. *Biophys. J.* 112:2624–2633.

61. De La Cruz, E. M., J. Roland, …, J. L. Martiel. 2010. Origin of twist-bend coupling in actin filaments. *Biophys. J.* 99:1852–1860.

62. De La Cruz, E. M., and M. L. Gardel. 2015. Actin mechanics and fragmentation. *J. Biol. Chem.* 290:17137–17144.

63. De La Cruz, E. M., J. L. Martiel, and L. Blanchoin. 2015. Mechanical heterogeneity favors fragmentation of strained actin filaments. *Biophys. J.* 108:2270–2281.

64. Otterbein, L. R., P. Graceffa, and R. Dominguez. 2001. The crystal structure of uncomplexed actin in the ADP state. *Science.* 293:708–711.

65. Graceffa, P., and R. Dominguez. 2003. Crystal structure of monomeric actin in the ATP state. Structural basis of nucleotide-dependent actin dynamics. *J. Biol. Chem.* 278:34172–34180.

66. Chu, J. W., and G. A. Voth. 2005. Allostery of actin filaments: molecular dynamics simulations and coarse-grained analysis. *Proc. Natl. Acad. Sci. USA.* 102:13111–13116.

67. Fan, J., M. G. Saunders, …, G. A. Voth. 2013. Molecular origins of cofilin-linked changes in actin filament mechanics. *J. Mol. Biol.* 425:1225–1240.

68. Plimpton, S. 1995. Fast parallel algorithms for short-range molecular-dynamics. *J. Comput. Phys.* 117:1–19.

69. Hammond, G. S. 1955. A correlation of reaction rates. *J. Am. Chem. Soc.* 77:334–338.

70. Dinner, A. R., and M. Karplus. 1999. Is protein unfolding the reverse of protein folding? A lattice simulation analysis. *J. Mol. Biol.* 292:403–419.

71. Alemany, A., B. Rey-Serra, …, F. Ritort. 2016. Mechanical folding and unfolding of protein barnase at the single-molecule level. *Biophys. J.* 110:63–74.

72. Alemany, A., and F. Ritort. 2017. Force-dependent folding and unfolding kinetics in DNA hairpins reveals transition-state displacements along a single pathway. *J. Phys. Chem. Lett.* 8:895–900.

73. Chou, S. Z., and T. D. Pollard. 2018. Mechanism of actin polymerization revealed by cryo-em structures of actin filaments with three different bound nucleotides. *bioRxiv* https://doi.org/10.1101/309534.

74. Tran, Q. H., and G. Unden. 1998. Changes in the proton potential and the cellular energetics of Escherichia coli during growth by aerobic and anaerobic respiration or by fermentation. *Eur. J. Biochem.* 251:538–543.

75. Wackerhage, H., U. Hoffmann, …, J. Zange. 1998. Recovery of free ADP, Pi, and free energy of ATP hydrolysis in human skeletal muscle. *J. Appl. Physiol.* 85:2140–2145.

76. Buchete, N. V., and G. Hummer. 2008. Coarse master equations for peptide folding dynamics. *J. Phys. Chem. B.* 112:6057–6069.

77. Suarez, C., J. Roland, …, L. Blanchoin. 2011. Cofilin tunes the nucleotide state of actin filaments and severs at bare and decorated segment boundaries. *Curr. Biol.* 21:862–868.

Biophysical Journal, Volume *115*

Supplemental Information

Insights into the Cooperative Nature of ATP Hydrolysis in Actin Filaments

Harshwardhan H. Katkar, Aram Davtyan, Aleksander E.P. Durumeric, Glen M. Hocky, Anthony C. Schramm, Enrique M. De La Cruz, and Gregory A. Voth

Supporting Material

Insights into the cooperative nature of ATP hydrolysis in actin filaments

Harshwardhan H. Katkar,[1] Aram Davtyan,[1] Aleksander E. P. Durumeric,[1] Glen M. Hocky,[1] Anthony C. Schramm,[2] Enrique M. De La Cruz,[2] Gregory A. Voth[1,*]

Affiliations:

[1]Department of Chemistry, Institute for Biophysical Dynamics, and James Franck Institute, University of Chicago, Chicago, IL, USA.

[2]Department of Molecular Biophysics and Biochemistry, Yale University, New Haven, CT, USA.

UCG MODEL

The UCG model was parameterized using three all-atom actin filament simulation trajectories corresponding to the three states of the bound nucleotide. Details of the all-atom simulations are provided below.

All-atom simulations

All-atom simulations of periodic actin filaments were performed in Gromacs (version 5.1.4)(1), using a protocol similar to Ref. (2). Briefly, a single actin subunit based on the Oda structure (Protein Data Bank structure 2ZWH) (3), consisting of a particular state of the bound nucleotide (either ATP, ADP-P_i or ADP, the former two were obtained by replacing the nucleotide ADP in the Oda structure with existing equilibrated simulations of ATP and ADP-P_i bound actin, with positions of replaced nucleotides found by aligning positions of actin subunits between the two (4)) was repeated along with a shift of 27.59 Å and a rotation of 166.6°, such that 13 repetitions of the subunit formed a single semi-periodic repeat of the actin helical structure. The simulation box was chosen such that the filament interacted with its own image in the periodic z-direction, mimicking a virtually infinite length filament. The system was solvated with TIP3P water and neutralized using salt ions, both of these tasks performed using VMD (5). The energy of the system was minimized, followed by gradual heating to increase the temperature from 0 K to 310 K, using the molecular dynamics code NAMD (6). The system was equilibrated at a temperature of 310 K and a pressure of 1 atm, until the root-mean-square deviation of the entire filament from its initial configuration reached a plateau. Production runs were performed using the terminal state of the system during equilibration, using the v-rescale thermostat (7) and the Parrinello-Rahman barostat implemented in Gromacs. The CHARMM27+CMAP force-field was used in these simulations (8).

Three AA simulation trajectories were obtained, one for a pure ATP bound actin filament, one for a pure ADP-P_i bound actin filament, and one for a pure ADP bound actin filament. Each of these AA trajectories was used to obtain CG models for the filaments with corresponding states of the bound nucleotide.

Pair-wise interactions

The pair-wise interactions between CG beads were divided into two categories, the intra-subunit interactions and the inter-subunit interactions. The intra-subunit interactions, between CG bead i and j at a distance r_{ij} belonging to the same actin subunit, were modeled using the harmonic potential U_b, as

$$U_b(r_{ij}) = k(r_{ij} - b)^2. \tag{1}$$

Here, k and b are the bond stiffness and zero energy bond length respectively. The inter-subunit interactions, between CG beads belonging to two different actin subunits, were modeled using inverted Gaussian interaction potential U_G, as

$$U_G(r_{ij}) = \frac{H}{\sigma_h\sqrt{2\pi}} \exp\left[-\frac{(r_{ij} - r_{mh})^2}{2\sigma_h^2}\right], \tag{2}$$

where parameters H and σ_h govern the depth and width, and are related to the bond stiffness in the harmonic potential, while r_{mh} governs the position of the minimum of the potential and is related to the equilibrium bond length in the harmonic potential.

Interaction parameters between a pair of CG particles with the same nucleotide state were obtained by constructing a hetero-elastic network model (hENM) based on the underlying all-atom simulations of pure state filaments. The parameters k and b for all pairs of intra-subunit CG beads were obtained from the hetero-elastic network model. The parameters H, σ_h and r_{mh} for all pairs of inter-subunit CG beads were obtained by least-square fitting of the corresponding harmonic potential U_b, obtained from the hENM, to the inverted Gaussian interaction potential U_G in the

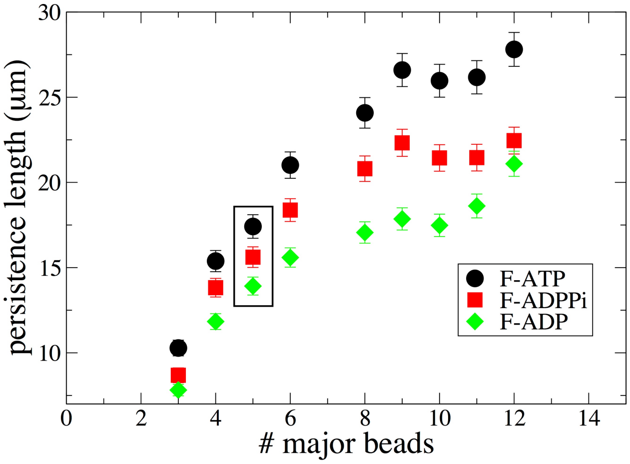

Figure S1: Persistence length of ATP, ADP-P$_i$ and ADP bound actin filaments, as a function of the number of major beads. The major beads are chosen in the order of increasing CG indices.

region where $U_b \leq 3$ kcal/mol. The inter-subunit beads interacted with springs only between a subset of CG sites that we call *major beads* and these inter-subunit springs were restricted to bead pairs that are up to two actin subunits apart in the filament.

Figure S1 shows the variation in persistence length for the three states of bound nucleotide, obtained from the coarse-grained model simulated in LAMMPS MD software (9) using Langevin dynamics. Each data-point was calculated as an average over five simulation runs, with each initiated using a different seed for random force and initial velocity generation. For a given state of bound nucleotide, the filament became more flexible as the number of major beads decreased.

Since the persistence length with 5 major beads (corresponding to CG bead indices 1 to 5 in Figure 1 of main text) agreed best with known persistence lengths in the literature, 5 major beads were used in the rest of the manuscript. Given the difficulty in accurately measuring persistence length in experiments and the wide range of experimental values reported in literature that varies with solution conditions, we picked a value that is consistent with the reported range (10-18). The 5 major beads in an actin subunit roughly correspond to the four major sub-domains in actin and the D-loop region (see Figure 1 of main text). The D-loop region inserts into actin's barbed end "target binding cleft" and is an important mediator of longitudinal interactions in the filament (4, 13, 19-23). This provided additional motivation for including at least these 5 major beads in our model. Note that the dependence of persistence length on the number of major beads seen from Figure S1 was specific to the choice of restricting inter-subunit springs to be between subunits that were up to two subunits apart in the filament. Further, based on our previous work (14), the persistence length was expected to increase with the number of major beads as equivalent CG bead pairs had identical springs between them in our model. Thus, each subunit of a given nucleotide state experienced the same force-field. Although including heterogeneity in the force-field similar to Ref. (14) would result into a more stable persistence length across different major beads, it would increase complexity of the resulting model since conformational behavior of each subunit would be different in a heterogeneous filament.

Pair-wise interactions for the mixed state

The nucleotide discrete state dynamics of actin subunits in the filament is allowed by the UCG model. Thus, during a particular simulation run, a given subunit can change its state from ATP to ADP-P$_i$ and from ADP-P$_i$ to ADP. This leads to the possibility of frequently observing several different combinations of the nucleotide states for neighboring subunits in a filament.

In our model, the pair-wise interactions were limited to be between subunits that are up to two neighbors apart along the filament. The pair-wise interactions between CG beads of neighboring subunits in the same state, say both ATP, were obtained by constructing a hENM using all-atom simulations of the ATP bound actin filament (pure state), and converting to Gaussian potentials. Similarly, pair-wise interactions between CG beads, both belonging to ADP-P$_i$ (or ADP) bound subunits were obtained from all-atom simulations of ADP-P$_i$ (or ADP) bound actin filaments, respectively. However, when the two CG beads belong to subunits bound to dissimilar nucleotides, the pair-wise interactions were not obtained directly from all-atom simulations via direct hENM parametrization. Generally, hENM parametrization captures fluctuations in the positions of CG beads; however, the nearby neighbors of a mixed nucleotide state filament likely influence such fluctuations. A suitable parametrization assuming a reasonable number of spring types would average over all such possible nucleotide state combinations of neighbors. However, exhaustively performing all-atom simulations of different combinations of nucleotide states in the filament is computationally prohibitive. Given that each CG bead belonging to a subunit can interact with another CG bead belonging to one of five consecutive subunits (including other CG beads within the same subunit), there are 3^5=243 possible combinations of nucleotide states between five consecutive subunits along the filament that are need to be simulated at the least. Moreover, the pure state all-atom simulations consist of a periodic filament with 13 identical copies of actin subunit. To generate statistics of equivalent quality, 13 copies of each of the 243 possible combinations of nucleotide states are required to be simulated. To reduce this multi-body complexity to a significant degree, we used a mixing rule to create parameters controlling mixed state interactions from pure state filament parameters. Specifically, in this *mixing* approach, we averaged the intra-subunit interaction parameters (H, σ_h and r_{mh}) from the pure state filaments to obtain parameters for the mixed state. For example, given a CG bead i belonging to an ADPPi bound subunit, and a CG bead j belonging to an ADP bound subunit, the parameter $\sigma_h^{Mix}(i,j)$ between them was obtained as

$$\sigma_h^{Mix}(i,j) = 0.5[\sigma_h(\mathrm{ATP}, i, j) + \sigma_h(\mathrm{ADP\text{-}P_i}, i, j)]. \tag{3}$$

To justify our mixing approach, we performed two additional short all-atom simulations of periodic actin filaments made of 26 subunits (with compositions 01001101000001010111110110 and 00010001110111000101100100 respectively, where 0=ADP-P$_i$, 1=ADP). These two filaments, in presence of the periodic boundary condition, consisted of all $2^5 = 32$ possible combinations of nucleotide states ADP-P$_i$ and ADP in five consecutive subunits along the filament. An approximate true *average* potential was created by averaging the explicit hENM parameters of each pair (i, j) of CG beads in these filaments (transformed into inverted Gaussian interactions). The discrepancy between the mixing approach and this approximate average potential is summarized in Figure S*2*. We define a mismatch parameter that measures the discrepancy between the force-field parameter σ_h for a pair of CG beads (i, j) derived using the mixing approach

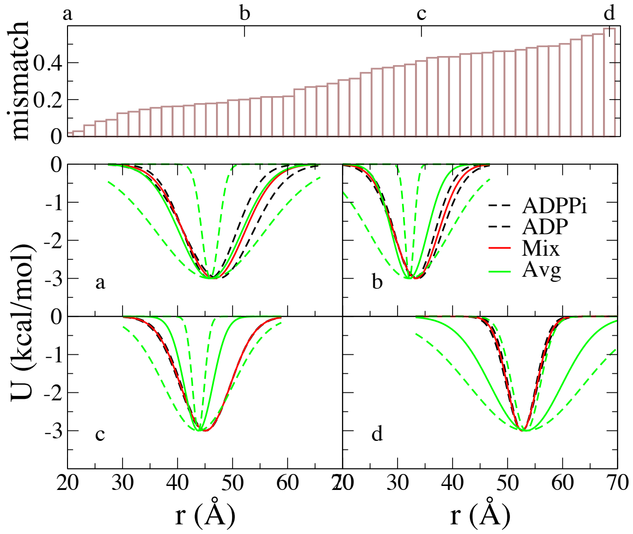

Figure S2: Comparison of the CG pair-wise interaction parameters obtained by using the mixing approach with those in average potential obtained from in the short all-atom simulations. Top panel shows the mismatch parameter, a measure for the difference in pair-wise interaction parameter σ_h obtained by the mixing approach and those in the average potential. The bottom four panels show the interaction potential between four sets of pairs of CG beads belonging to neighboring subunits, corresponding to lowest (panel a), two intermediate (panels b and c) and the largest (panel d) mismatch values (marked with a,b,c and d in the top panel). The interaction potential between a CG bead i belonging to an ADP-P$_\text{i}$ bound subunit and a CG bead j, belonging to a ADP bound subunit obtained by using the mixing approach is shown in red, with the corresponding pure state potentials shown as dotted black curves, and the average potential from short all-atom simulations is shown in solid green, with the potentials corresponding to ± 1 standard deviation in parameters H and σ_h shown with the dotted green curves.

$(\sigma_h^{Mix}(i,j))$ and that in the average potential obtained from the short all-atom simulations $(\sigma_h^{Avg}(i,j))$.

$$\text{mismatch}(i,j) = \frac{\left|\sigma_h^{\text{Avg}}(i,j) - \sigma_h^{\text{Mix}}(i,j)\right|}{\text{MAX}\left[\sigma_h^{\text{Avg}}(i,j), \sigma_h^{\text{Mix}}(i,j)\right]} \tag{4}$$

Here, σ_h is the inverted Gaussian interaction parameter that characterizes the steepness of the potential energy (Equation (2)). The top panel in Figure S2 shows the mismatch parameter for all pairs of interacting CG beads in our model, plotted with increasing values of the mismatch parameter. Clearly, the mismatch was observed to be small for many pairs of CG beads, but was significant for certain CG bead pairs towards the right-hand side of the plot.

Parameters of the inverted Gaussian interaction for a pair of CG beads in the average potential obtained from the short all-atom simulations varied significantly owing to different combinations of bound nucleotides of the rest of their neighboring subunits along the filament. We calculate the average and standard deviation of the parameters H and σ_h along the filament for each pair of CG beads corresponding to a distinct nucleotide pair. The four panels a, b, c and d on the bottom show the form of the inverted Gaussian potential obtained with the mixing approach and that in the average potential, corresponding to the four pairs of CG beads marked in the top panel (a corresponds to the lowest mismatch, d corresponds to the highest mismatch, and b and c correspond to the intermediate mismatch). It can be seen that even for the pair of CG beads corresponding to the largest mismatch, the potential obtained using the mixing approach was within the variation in the average potential (corresponding ± 1 standard deviation in parameters H and σ_h, shown as dotted green lines in Figure S2) obtained from the all-atom simulations. Given the huge computational advantage balanced by the reasonable accuracy of our rather simple mixing approach, we used it in the rest of this work to obtain interactions between a pair of CG beads corresponding to distinct nucleotide states, acknowledging that alternative choices are possible.

UCG PARAMETER INTERPRETATION

The formulas presented for UCG transitions inherently have a large bearing on the results of the current study. It is therefore useful to note natural assumptions which could produce the rules used. While ideally one would like to know exactly the instantaneous rates as a function of monomer configuration, we do not have access to this data. Instead, we are forced to infer the dependence of a transition probability based on the configuration of the system. We chose to do so by primarily assuming that, for example, the transition state free energy controlling the rate of F-ATP→F-ADP-P_i tracks the pointwise free energy of either the reactants or the products as the configuration of the system changes (i.e. as the reactant free energy changes, the transition state free energy changes similarly). Importantly, if the transition state stability has the same dependence on configuration as the reactants do, then the instantaneous rate of the forward reaction does not change (as it is controlled by the difference in these two energies, and as such will stay constant). Contrastingly, if the stability of the transition state instead follows the products, then the forward reaction will change rate as the protein changes configuration, but the rate of the reverse reactions will stay constant as configuration changes. These concepts are close to the kinetic implications of the Hammond postulate in organic chemistry (24).

Hammond-type dependence has been observed for macroscopic rates and environmental dependence in complex reactions (e.g. protein folding and unfolding (25, 26), and more recently DNA hairpin folding and unfolding (27)). It should be noted that the Metropolis-Hastings criteria was chosen as a convenient approximation which one can interpret via transition states: the cooperativity seen derives from a fluctuating pocket around ATP which moves ATP towards a relatively static barrier. Additionally, the dependence proposed in our study does match the detailed information gained upon flattening actin in our earlier QM/MM studies (28, 29). Unfortunately, no such data is known for phosphate release. The conclusions made in this study primarily focus on the extent of nonlocality observed at the resolution of the MSM and not the fine-grained details of the cooperativity. Clearly, if the individual monomers in the filament did not "feel" the state of a given neighboring monomer, no cooperativity would be observed in the current study. As such, the main conclusions are robust to the exact conformational dependence of the rate imposed.

Whether the transition state stability primarily follows the stability of the reactants or products in the UCG model depends on the parameters of the model and the specific filament configuration considered (additional complexity on the transition state stability is introduced via the dihedral dependence parameters). In the following discussion, we will consider $i \rightarrow j$ the forward reaction. The conditional statement in the Metropolis-Hastings-like rate law switches between the two transition state cases. Specifically, the following conditional

$$\mathrm{MIN}\left[\frac{k_{j\to i}(\phi)}{k_{i\to j}(\phi)}\exp\left[-\beta\left(U_j - U_i\right) - \epsilon_{ij}\right], 1\right]$$

divides our configurational phase space into two sets, with one set satisfying

$$\frac{k_{j\to i}(\phi)}{k_{i\to j}(\phi)}\exp\left[-\beta\left(U_j - U_i\right) - \epsilon_{ij}\right] < 1$$

and the other set defined as its complement. This condition can be rearranged giving

$$-\beta\left(U_j - U_i\right) - \epsilon_{ij} - \log\frac{[0.5 + 0.5\tanh\eta(\phi - \phi_0)]}{[0.5 - 0.5\tanh\eta(\phi - \phi_0)]} < \log\frac{k^0_{i\to j}}{k^0_{j\to i}}$$

Note that when no additional dihedral dependence is added (i.e. $\eta = 0$) the third term on the left side is zero. Roughly, a highly endergonic reaction ($U_j - U_i \gg 0$) forces the transition state to follow the products in stability. More specifically, assuming our rates can be expressed modulo a proportionality constant similarly to the following form from transition state theory, with U denoting free energy and ‡ denoting transition state values

$$\exp\left[-\beta(U^{\ddagger}_{i,j} - U^{corr}_{i})\right]$$

we find that we can express the energy of our transition state (modulo a constant) in our first set (that satisfying the given conditional) as

$$U^{\ddagger}_{i,j} = U^{\mathrm{corr}}_{j} - k_B T \log k_{j\to i}(\phi), \tag{5}$$

where we have assumed that ϵ_{ij} has been incorporated into either U_j or U_i giving corrected energies U^{corr}_j and U^{corr}_i. Importantly, the inverse reaction in the first set shares the same transition state energy; however, as its local energy is given by U^{corr}_j, the rate no longer takes this term into account. While we have only considered the first set in phase space in this paragraph, the second set enjoys the same relations with the role of reactants and products reversed and the appropriate parameters swapped out. The switching point in the transition state behavior is affected by all parameters, but is controlled in practice by setting ϵ_{ij} while other parameters are modified. Additional parameters, e.g. $k^0_{j\to i}$, modify the constant offset in energy and dihedral dependence of the transition state, and η controls the sharpness of the dihedral dependence.

UCG PARAMETER ESTIMATION

There are three parameters in the UCG model for each of the reactions F-ATP $\rightleftharpoons$ F-ADP-P$_i$ and F-ADP-P$_i$ $\rightleftharpoons$ F-ADP + P$_i$. The prefactor $k^0_{i\to j}$ in absence of the dihedral dependence corresponds to the rate of attempting a subunit from state i to final state j. Here $i, j \in$ [ATP, ADP-Pi, ADP]. The prefactor for the corresponding quantity in the reverse reaction is $k^0_{j\to i}$. The third parameter, Metropolis-Hasting correction factor ϵ_{ij}, was added to account for the lack of a common reference state for the internal energy of the two states.

In the following discussion, $\langle\cdot\rangle$ denotes an average quantity. We need three constraints in order to estimate the three parameters. Two of these constraints are given through matching average values $\langle K_{i\to j}\rangle$ and $\langle K_{j\to i}\rangle$ with known forward and reverse macroscopic rates of reactions $R_{i\to j}$ and $R_{j\to i}$ respectively. The forward macroscopic rate $R_{i\to j}$ of the reaction F-ATP ⇌ F-ADP-P$_i$ is 0.3 s^{-1} and that for the reaction F-ADP-P$_i$ ⇌ F-ADP + P$_i$ is 0.0068 s^{-1}. The estimated Gibbs free energy for the reaction F-ATP ⇌ F-ADP-P$_i$ calculated using metadynamics simulations, ΔG is in the range of -3 to -6 kcal/mol (28, 29). The estimates for the total change in Gibbs free energy for the net reaction F-ATP ⇌ F-ADP + P$_i$ under physiological conditions varies in a much wider range (30, 31). We chose $\Delta G = -3.2$ kcal/mol for the reaction F-ATP ⇌ F-ADP-P$_i$, and $\Delta G = -5.5$ kcal/mol for the reaction F-ADP-P$_i$ ⇌ F-ADP + P$_i$. These values of ΔG were used to calculate the reverse reaction macroscopic rates $R_{j\to i}$, using the relationship

$$R_{j\to i} = R_{i\to j}\exp[\beta\Delta G] \tag{6}$$

Due to lack of additional relevant information from the atomistic simulations and from experiments, we imposed the third constraint by specifying the average value of the acceptance probability for the forward reaction sampled in our simulations.

$$\langle p_{i\to j}\rangle \to 0.1 \tag{7}$$

The motivation behind choosing a small average probability of acceptance for the forward reaction was to make the state transitions sensitive towards the potential energy difference between the two states. As $\langle p_{i\to j}\rangle \to 1$, the transitions $i \to j$ become insensitive to the potential energy difference, and the instantaneous transition rate for the forward reaction is simply given by the rate of attempting. The arbitrarily specified value affects the sensitivity of the reaction rates towards the potential energy difference, which in turn depends on the states of neighboring subunits and affects the degree of cooperativity observed in our UCG simulations. Acknowledging this dependence, we used a parameter X later in our kinetic model to vary the extent of the observed cooperativity.

To summarize, the three constraints are

$$\begin{gathered}
\langle K_{i\to j}\rangle = k^0_{i\to j}\left\langle [0.5 + 0.5\tanh\eta(\phi-\phi_0)]\mathrm{MIN}\left[\frac{k_{j\to i}(\phi)}{k_{i\to j}(\phi)}exp\left[-\beta\left(U_j - U_i\right) - \epsilon_{ij}\right], 1\right]\right\rangle \to R_{i\to j} \\
\langle K_{j\to i}\rangle = k^0_{j\to i}\left\langle [0.5 - 0.5\tanh\eta(\phi-\phi_0)]\mathrm{MIN}\left[\frac{k_{i\to j}(\phi)}{k_{j\to i}(\phi)}exp\left[-\beta\left(U_i - U_j\right) + \epsilon_{ij}\right], 1\right]\right\rangle \to R_{j\to i} \\
\langle p_{i\to j}\rangle = \left\langle \mathrm{MIN}\left[\frac{k_{j\to i}(\phi)}{k_{i\to j}(\phi)}\exp\left[-\beta\left(U_j - U_i\right) - \epsilon_{ij}\right], 1\right]\right\rangle \to 0.1
\end{gathered} \tag{8}$$

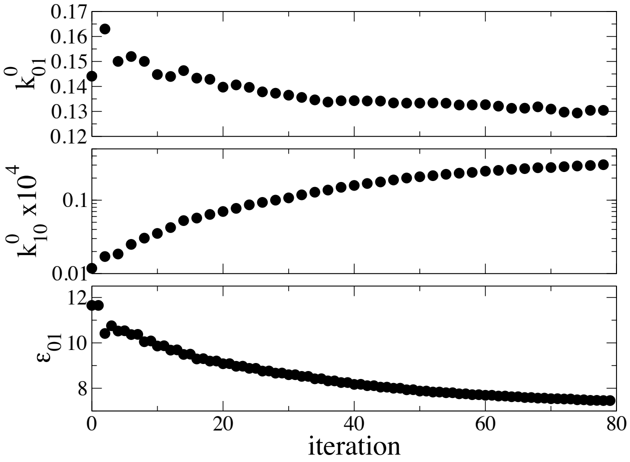

Figure S3: Iterations to obtain the UCG parameters for the reaction F-ATP $\rightleftharpoons$ F-ADP-P$_i$, for $\eta = 0.125$.

Let x_1 be the fraction of the number of times in a simulation run that MIN $\left[\frac{k_{j\to i}(\phi)}{k_{i\to j}(\phi)}\exp[-\beta(U_j - U_i) - \epsilon_{ij}], 1\right] = 1$, and x_2 be the fraction otherwise. The above equations give the following update rules for parameter optimization,

$$\begin{aligned} k^{0,*}_{i\to j} &= k^{0,n}_{i\to j}\frac{R_{i\to j}}{\langle K_{i\to j}\rangle} \\ k^{0,*}_{j\to i} &= k^{0,n}_{j\to i}\frac{R_{j\to i}}{\langle K_{j\to i}\rangle} \end{aligned} \tag{9}$$

$$\epsilon^*_{ij} = \epsilon^n_{ij} + \ln\left[\frac{0.1 - x_1}{x_2\left\langle\left[\frac{k_{j\to i}(\phi)}{k_{i\to j}(\phi)}exp[-\beta(U_j - U_i) - \epsilon^n_{ij}]\right]\right\rangle_{\neq 1}}\right] \tag{10}$$

These equations provided a way of performing iterations to optimize the UCG parameters. At iteration n, the following set of update rules was used to obtain a new guess for the parameters.

$$\begin{aligned} k^{0,n+2}_{i\to j} &= \omega k^{0,*}_{i\to j} + (1-\omega)k^{0,n}_{i\to j} \\ k^{0,n+2}_{j\to i} &= \omega k^{0,*}_{j\to i} + (1-\omega)k^{0,n}_{j\to i} \end{aligned} \tag{11}$$

Similarly,

$$\epsilon^{n+1}_{ij} = \omega\epsilon^*_{ij} + (1-\omega)\epsilon^n_{ij} \tag{12}$$

For efficiency, we skipped iterating for $k^0_{i\to j}$ and $k^0_{j\to i}$ in every odd numbered iteration.

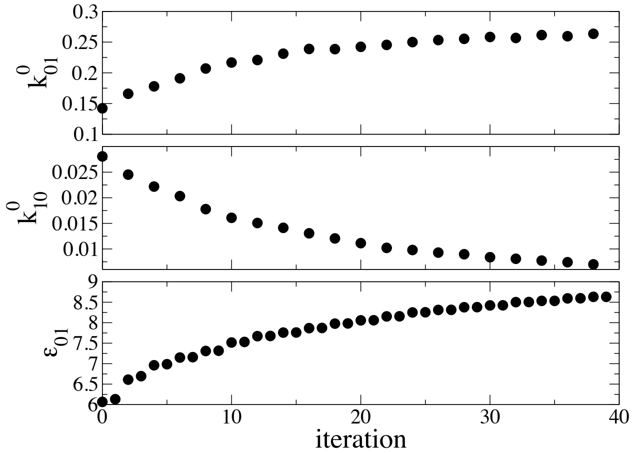

Figure S4: Iterations to obtain UCG parameters for the reaction F-ADP-P_i ⇌ F-ADP + P_i, for $\eta = 0$.

ATP hydrolysis

For the reaction F-ATP ⇌ F-ADP-P_i, we constructed a long (1040 subunits) F-ATP filament. An initial guess for the UCG parameters was made, making sure that $\langle p_{i \to j} \rangle < 0.1$. For the first iteration $n = 1$, the UCG simulation was run for a sufficiently long time such that all the subunits underwent the forward state transition from ATP (denoted by 0) to ADP-P_i (denoted by 1) at least once, and about $\sim O(10)$ subunits also underwent the reverse state transition. The mean first passage time for the forward and reverse transitions was calculated from these transitions, and was used as an estimate for the inverse of the average transition rates of the corresponding reactions in Equation (4), $\langle K_{i \to j} \rangle^{-1}$ and $\langle K_{j \to i} \rangle^{-1}$ respectively. For faster sampling, a pseudo-UCG simulation was run, such that at each step in the simulation, the term in the denominator of Equation (10) was evaluated for the state transition. However, instead of changing the state of the subunit to ADP-P_i like in regular UCG simulations, it was kept unchanged in the pseudo-UCG simulations.

For efficient sampling of both forward and reverse transition events, we carefully scaled our target macroscopic rates as follows. We used a common scaling factor of 50×10^{-5} to convert the forward and reverse rates from s^{-1} to $step^{-1}$. Thus, the target forward macroscopic rate was $R_{i \to j} = 1.5 \times 10^{-4}$ transitions per step, while the target reverse macroscopic rate was $R_{j \to i} = 8.8 \times 10^{-7}$ transitions per step (Figure S3).

P_i release

A similar procedure was followed to obtain UCG parameters for the P_i release reaction. A common scaling factor of 50×10^{-3} was used to convert the forward and reverse rates from s^{-1} to $step^{-1}$ in our simulations, for efficient sampling of both forward and reverse transition events. The resulting target values were $R_{i \to j} = 3.4 \times 10^{-4}$ transitions per step for the forward macroscopic rate and $R_{j \to i} = 4.5 \times 10^{-8}$ transitions per step for the reverse macroscopic rate (Figure S4).

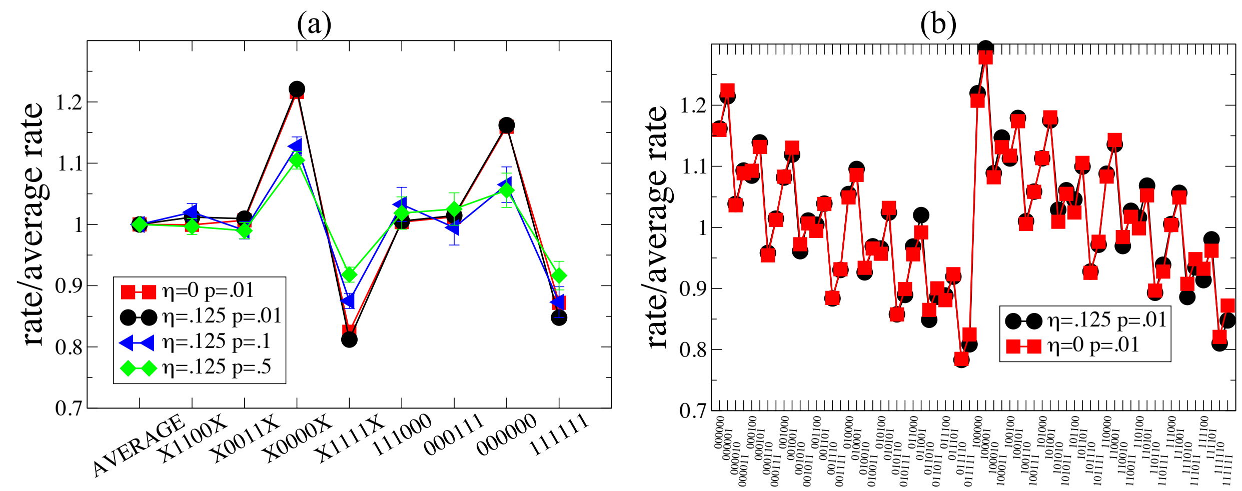

Figure S5: Multi-body effect in ATP hydrolysis, plotted as a ratio of the conditional rate with the average rate. Combinations of neighboring monomer states are indicated using a key on the x-axis, that denotes the state (0=unhydrolyzed, 1=hydrolyzed, X=either) of each of the neighboring subunits, starting from the third neighbor in the pointed-end direction to the third neighbor in the barbed-end direction. (a) Specific combinations of neighbors and (b) all 64 possible combinations of neighbors. Different colors and symbols correspond to different choices of the dihedral angle dependence parameter η and average acceptance probability p, as indicated in the legend. The multi-body effect in ATP hydrolysis is symmetric with respect to the two ends of the filament. Thus, for example, the enhancement in rate for 111000 is approximately equal to that for 000111.

PARAMETER CHOICE AND COOPERATIVITY

In the following section, we demonstrate the effect of choices we made for remaining parameters on the cooperativity observed.

ATP hydrolysis

Figure S5 shows the variation in the multi-body cooperative effect predicted by the UCG model for the ATP hydrolysis reaction, as a function of (a) the presence or absence of the explicit dihedral angle dependence, modulated using η, and (b) the target value of $\langle p_{i\to j}\rangle$ used for UCG parameter estimation. While the former does not significantly affect the predicted cooperativity, the latter was expected to serve as a handle to control the extent of cooperativity. As expected from the form of Equation (8), decreasing $\langle p_{i\to j}\rangle$ increased the model's sensitivity towards multi-body effects.

Figure S6 shows similar variation in the multi-body cooperative effect predicted by the UCG model for the P_i release reaction, as a function of the value of $\langle p_{i\to j}\rangle$ used for UCG parameter estimation. Figure S7 shows the P_i release rate variation for all the combinations of neighboring states studied.

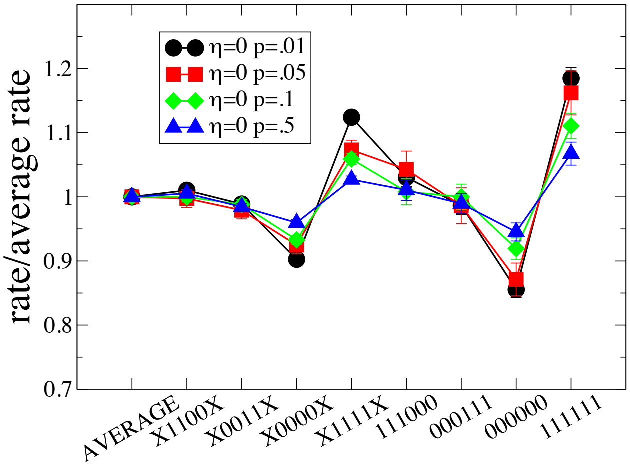

Figure S6: Multi-body effect in P_i release plotted as a ratio of the conditional rate to the average rate. The key on the x-axis is similar to that described in Figure S5 (except for the new definitions 0=ADP-P_i, 1=ADP). Different colors and symbols indicate different values of the average acceptance probability p as indicated in the legend.

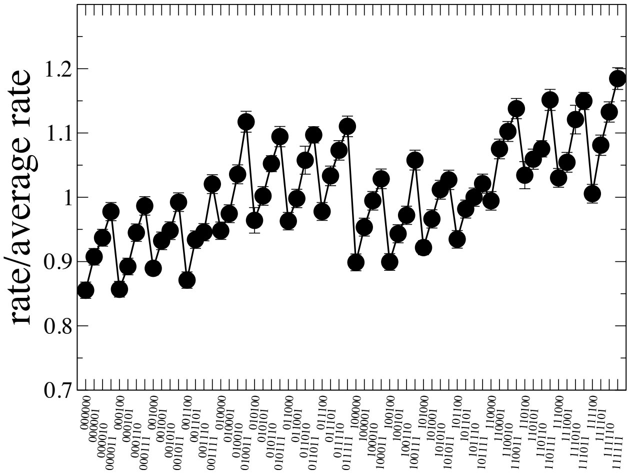

Figure S7: Multi-body effect in P_i release plotted as a ratio of the conditional rate to the average rate for all 64 possible combination of nucleotide states of neighboring subunits. The key on the x-axis is similar to that described in Figure S5. Error bars indicate the standard error for each data-point. The multi-body effect in P_i release is symmetric with respect to the two ends of the filament.

MARKOV STATE MODEL

The kinetic model used in this work is similar to that commonly used in the literature (32, 33), and consisted of the following elementary reactions.

1. Polymerization at the barbed end
2. De-polymerization at the barbed end
3. De-polymerization at the pointed end (only in the conserved system)
4. ATP hydrolysis
5. P_i release

We assumed that transitions associated with (de-)polymerization reactions at the barbed end, de-polymerization reactions at the pointed end, and internal reaction events at each monomer were independent when considering single transitions through the MSM state space. The rates of these transitions, however, each depended on the state vector itself. Let $K_{\text{pol.}}$ denote the polymerization rate, $K_{\text{dis.,barbed}}$ denote the de-polymerization rate at the barbed end, while $K_{\text{dis.,pointed}}$ denote that at the pointed end. Also let $K_{\text{hyd.}}$ and $K_{\text{rel.}}$ denote rates of ATP hydrolysis and P_i release respectively. $K_{\text{dis.,barbed}}$ and $K_{\text{dis.,pointed}}$ are dependent on the state of the terminal subunit at the barbed end and the pointed end respectively. Using the values of these reaction rates provided in Table 1 of the manuscript, the system evolved using a Monte Carlo algorithm with a constant time-step.

The initial condition was chosen such that there are $n_0$subunits present in the filament. The corresponding sequence of states of the nucleotides was stored in a state vector $s[n_0]$ of size n_0. The initial free actin monomer concentration was chosen to be c_0. Let n deote the length of the filament and c denote the free actin monomer concentration at time t. The time-step was chosen as dt and the system is updated at time $t + dt$ based on its state at time t, as follows:

1. A random number uniformly distributed between the interval [0,1] was generated for the barbed-end of the filament.
    a. If the random number was between 0 and $dt \times c \times K_{\text{pol.,}}$ the polymerization reaction was selected. The length of the filament was updated to $n + 1$ The vector $s[n]$ was expanded to $s[n + 1]$, with the new sequence of states of the nucleotide stored in it.
    b. If the random number was between $dt \times c \times K_{\text{pol.}}$ and $dt \times c \times K_{\text{pol.}} + dt \times K_{\text{dis.,barbed}}$, then the de-polymerization reaction was chosen. The length of the filament was changed to $n - 1$ The vector $s[n]$ was reduced to $s[n - 1]$, with the new sequence of states of the nucleotide stored in it.
2. A uniform random number was generated for the pointed-end of the filament.
    a. If the random number was between 0 and $dt \times K_{\text{dis.,pointed}}$, then the de-polymerization reaction at the pointed end was chosen. The length of the filament was changed to $n - 1$. The vector $s[n]$ was reduced to $s[n - 1]$, with the new sequence of states of the nucleotide stored in it.
3. A set of $n - 2$ uniform random numbers was generated, one for each of the interior subunits in the filament. For each subunit m, the entry $s[m]$ was updated if the random number was between 0 and $dt \times K_{\text{react}}$, where $K_{\text{react}} = K_{\text{hyd.}}$ if the state of the subunit was ATP, and $K_{\text{react}} = K_{\text{rel.}}$ if the state of the subunit was ADP-P_i.

In the above, the rates $K_{\text{hyd.}}$ and $K_{\text{rel.}}$ were modulated according to state of neighboring monomers, depending on the degree of cooperativity considered. The cooperativity was not considered for the two terminal monomers (excluding the filament ends) on each side of the filament. In other words, these monomers reacted with the average rates of ATP hydrolysis and P_i release. In the conserved system, the value of c was updated after each de-polymerization reaction took place.

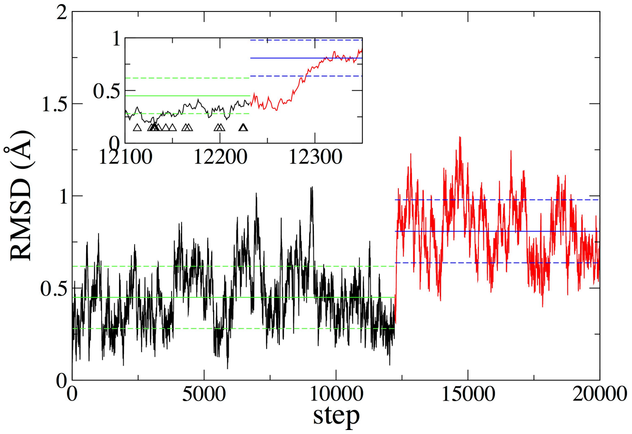

Figure S8: A transition event corresponding to phosphate release in a single subunit from a short simulation run. The simulation setup is similar to that used in obtaining Figure 4 and Figure S7. The root-mean square displacement (RMSD) in positions of CG beads 1-4 of subunit 100 in the filament is shown as a function of simulation steps. The transition corresponding to phosphate release in subunit 100 takes place at step 12232. The RMSD before (black curve) and after (red curve) the transition are shown. The average RMSD before (green line) and after (blue line) the transition are also shown for clarity, along with the range of their variation (± 1 standard deviation, shown as dotted lines with corresponding colors). Inset shows the same data, highlighting the details near the transition event. Steps corresponding to unsuccessful transition attempts by subunit 100 are also shown (inset: black triangles). The subunit configuration reaches a new equilibrium at a faster rate compared to the rates of transition.

The value of dt was carefully chosen to be small enough such that all of the values ($dt \times c \times K_{\text{pol.}} + dt \times K_{\text{dis.,barbed}}$, $dt \times K_{\text{dis.,pointed}}$ and $dt \times K_{\text{react}}$ were significantly less than one at all times. Further modifications were made to the above model depending on the system being simulated, as explained in the manuscript.

MARKOV STATE MODEL DISCRETIZATION AND INTERPRETATION OF KINETICS

Many modern empirically parameterized Markov State Models use state space discretizations which are much finer than the model presented here (34, 35). Systematic analysis of said models has often focused on the quality of this discretization, i.e. the quality and accuracy of the MSM created with respect to the system it approximates. An intuitive metric for a high quality MSM is that the system loses memory when present in a single discrete state: transitions out of a discrete MSM state should not depend on the manner in which one entered said state. It can be seen that the CG configurational dynamics do decouple from the rate of large scale transitions relevant to the MSM derived (Figure S8). This decoupling also legitimizes the use of highly nonequilibrium trajectories for parametrization, as the system is effectively always in conditional equilibrium (36).

The model produced in this work solely aims to capture relaxation timescales which are characterized by the progression of hydrolysis, phosphate release, and (de-)polymerization, which are on the order of seconds or minutes. It is natural to ask how a model which takes into account molecular motions, even at a relatively coarse-grained level, can be propagated using molecular dynamics to see such kinetics. Specifically, we have assumed that the true behavior of the atomistic fluctuations in an actin filament orthogonal to the slow timescale events described in the previous

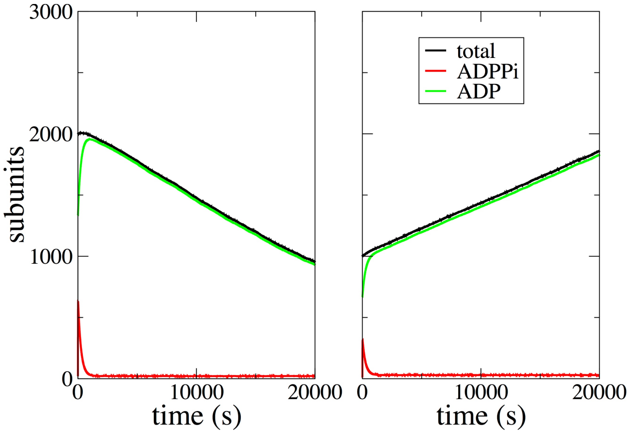

Figure S9: Average number of total subunits and subunits bound to nucleotides ADP-P_i and ADP in the filament as a function of time, for $X = 0$ (left panel, $c = 0.116$ μM) and above (right panel, $c = 0.120$ μM).

paragraph are effectively decoupled: The true biological polymer is assumed to achieve an equilibrium state conditional on the progress of these reactions. As result, the underlying *detailed* dynamics of the system conditional on these reactions is relatively unimportant: the system obeys laws similar to those underpinning transition state theory. Critically, while the CG conformational dynamics are likely dynamically inaccurate with respect to the discrete transitions simulated, they are still decoupled in their relaxation times. As a result, assuming the CG model is parameterized to reproduce equilibrium properties, we argue that configurational dependence on the observed hydrolysis rates are still valid.

FILAMENT DYNAMICS AT CONSTANT FREE ACTIN CONCENTRATION

Figure S9 shows the average contents (ADP-P_i bound and ADP bound subunits) of the filaments, obtained from 1000 statistical runs, as implied by the random hydrolysis mechanism. The initial filament consists of 2/3rd fraction of the filament near the pointed end being ADP bound and the reminder tip near the barbed end made of ATP bound subunits. After a quick initial transient from the chosen initial condition, a steady growth rate with a constant slope for the filament contents is obtained.

SUPPORTING REFERENCES

1. Van der Spoel, D., E. Lindahl, B. Hess, G. Groenhof, A. E. Mark, and H. J. C. Berendsen. 2005. GROMACS: Fast, flexible, and free. *J. Comput. Chem.* 26:1701-1718.
2. Saunders, Marissa G., and Gregory A. Voth. 2012. Comparison between actin filament models: Coarse-graining reveals essential differences. *Structure* 20:641–653.
3. Oda, T., M. Iwasa, T. Aihara, Y. Maeda, and A. Narita. 2009. The nature of the globular-to fibrous-actin transition. *Nature* 457:441-445.

4. Pfaendtner, J., D. Branduardi, M. Parrinello, T. D. Pollard, and G. A. Voth. 2009. Nucleotide-dependent conformational states of actin. *Proc. Natl. Acad. Sci. U.S.A.* 106:12723-12728.
5. Humphrey, W., A. Dalke, and K. Schulten. 1996. VMD: Visual molecular dynamics. *J. Mol. Graph. Model.* 14:33-38.
6. Phillips, J. C., R. Braun, W. Wang, J. Gumbart, E. Tajkhorshid, E. Villa, C. Chipot, R. D. Skeel, L. Kale, and K. Schulten. 2005. Scalable molecular dynamics with NAMD. *J. Comput. Chem.* 26:1781-1802.
7. Bussi, G., D. Donadio, and M. Parrinello. 2007. Canonical sampling through velocity rescaling. *J. Chem. Phys.* 126:014101.
8. Mackerell, A. D., M. Feig, and C. L. Brooks. 2004. Extending the treatment of backbone energetics in protein force fields: Limitations of gas-phase quantum mechanics in reproducing protein conformational distributions in molecular dynamics simulations. *J. Comput. Chem.* 25:1400-1415.
9. Plimpton, S. 1995. Fast parallel algorithms for short-range molecular-dynamics. *J. Comput. Phys.* 117:1-19.
10. Isambert, H., P. Venier, A. C. Maggs, A. Fattoum, R. Kassab, D. Pantaloni, and M. F. Carlier. 1995. Flexibility of actin-filaments derived from thermal fluctuations - effect of bound nucleotide, phalloidin, and muscle regulatory proteins. *J. Biol. Chem.* 270:11437-11444.
11. Chu, J. W., and G. A. Voth. 2006. Coarse-grained modeling of the actin filament derived from atomistic-scale simulations. *Biophys. J.* 90:1572-1582.
12. McCullough, B. R., L. Blanchoin, J. L. Martiel, and E. M. De La Cruz. 2008. Cofilin increases the bending flexibility of actin filaments: Implications for severing and cell mechanics. *J. Mol. Biol.* 381:550-558.
13. Pfaendtner, J., E. Lyman, T. D. Pollard, and G. A. Voth. 2010. Structure and dynamics of the actin filament. *J. Mol. Biol.* 396:252-263.
14. Fan, J., Marissa G. Saunders, and Gregory A. Voth. 2012. Coarse-graining provides insights on the essential nature of heterogeneity in actin filaments. *Biophys. J.* 103:1334–1342.
15. Schramm, A. C., G. M. Hocky, G. A. Voth, L. Blanchoin, J. L. Martiel, and E. M. De La Cruz. 2017. Actin filament strain promotes severing and cofilin dissociation. *Biophys. J.* 112:2624-2633.
16. De La Cruz, E. M., and M. L. Gardel. 2015. Actin mechanics and fragmentation. *J. Biol. Chem.* 290:17137-17144.
17. De la Cruz, E. M., J. L. Martiel, and L. Blanchoin. 2015. Mechanical heterogeneity favors fragmentation of strained actin filaments. *Biophys. J.* 108:2270-2281.
18. De La Cruz, E. M., J. Roland, B. R. McCullough, L. Blanchoin, and J. L. Martiel. 2010. Origin of twist-bend coupling in actin filaments. *Biophys. J.* 99:1852-1860.
19. Otterbein, L. R., P. Graceffa, and R. Dominguez. 2001. The crystal structure of uncomplexed actin in the ADP state. *Science* 293:708-711.
20. Graceffa, P., and R. Dominguez. 2003. Crystal structure of monomeric actin in the ATP state - structural basis of nucleotide-dependent actin dynamics. *J. Biol. Chem.* 278:34172-34180.
21. Chu, J. W., and G. A. Voth. 2005. Allostery of actin filaments: Molecular dynamics simulations and coarse-grained analysis. *Proc. Natl. Acad. Sci. U.S.A.* 102:13111-13116.

22. Fan, J., M. G. Saunders, E. J. Haddadian, K. F. Freed, E. M. De La Cruz, and G. A. Voth. 2013. Molecular origins of cofilin-linked changes in actin filament mechanics. *J. Mol. Biol.* 425:1225-1240.
23. Kang, H., M. J. Bradley, W. A. Elam, and E. M. De La Cruz. 2013. Regulation of actin by ion-linked equilibria. *Biophys. J.* 105:2621-2628.
24. Hammond, G. S. 1955. A correlation of reaction rates. *J. Am. Chem. Soc.* 77:334-338.
25. Dinner, A. R., and M. Karplus. 1999. Is protein unfolding the reverse of protein folding? A lattice simulation analysis. *J. Mol. Biol.* 292:403-419.
26. Alemany, A., B. Rey-Serra, S. Frutos, C. Cecconi, and F. Ritort. 2016. Mechanical folding and unfolding of protein barnase at the single-molecule level. *Biophys. J.* 110:63-74.
27. Alemany, A., and F. Ritort. 2017. Force-dependent folding and unfolding kinetics in DNA hairpins reveals transition-state displacements along a single pathway. *J. Phys. Chem. Lett.* 8:895-900.
28. McCullagh, M., M. G. Saunders, and G. A. Voth. 2014. Unraveling the mystery of ATP hydrolysis in actin filaments. *J. Am. Chem. Soc.* 136:13053-13058.
29. Sun, R., O. Sode, J. F. Dama, and G. A. Voth. 2017. Simulating protein mediated hydrolysis of ATP and other nucleoside triphosphates by combining QM/MM molecular dynamics with advances in metadynamics. *J. Chem. Theory Comput.* 13:2332-2341.
30. Tran, Q. H., and G. Unden. 1998. Changes in the proton potential and the cellular energetics of escherichia coli during growth by aerobic and anaerobic respiration or by fermentation. *Eur. J. Biochem.* 251:538-543.
31. Wackerhage, H., U. Hoffmann, D. Essfeld, D. Leyk, K. Mueller, and J. Zange. 1998. Recovery of free ADP, P-i, and free energy of ATP hydrolysis in human skeletal muscle. *J. Appl. Physiol.* 85:2140-2145.
32. Ranjith, P., K. Mallick, J.-f. Joanny, and D. Lacoste. 2010. Role of ATP-hydrolysis in the dynamics of a single actin filament. *Biophys. J.* 98:1418-1427.
33. Vavylonis, D., Q. Yang, and B. O'Shaughnessy. 2005. Actin polymerization kinetics, cap structure, and fluctuations. *Proc. Natl. Acad. Sci. U.S.A.* 102:8543-8548.
34. Prinz, J. H., H. Wu, M. Sarich, B. Keller, M. Senne, M. Held, J. D. Chodera, C. Schutte, and F. Noe. 2011. Markov models of molecular kinetics: Generation and validation. *J. Chem. Phys.* 134:174105.
35. Bowman, G. R., V. Pande, and F. Noe. 2014. An introduction to Markov state models and their application to long timescale molecular simulation. Springer, Dordrecht.
36. Nuske, F., H. Wu, J. H. Prinz, C. Wehmeyer, C. Clementi, and F. Noe. 2017. Markov state models from short non-equilibrium simulations-analysis and correction of estimation bias. *J. Chem. Phys.* 146:094104.